THESIS FOR THE DEGREE OF DOCTOR OF PHILOSOPHY

Quantum Theory of Exciton-Exciton Interactions in Atomically Thin Semiconductors

Daniel Erkensten

Department of Physics

Chalmers University of Technology

Göteborg, Sweden 2023

Quantum Theory of Exciton-Exciton Interactions in Atomically Thin Semiconductors

Daniel Erkensten

ISBN 978-91-7905-971-2
Doktorsavhandlingar vid Chalmers tekniska högskola
Ny serie nr 5437
ISSN 0346-718X

Department of Physics
Chalmers University of Technology
SE-412 96 Göteborg
Sweden
Telephone + 46 (0)31-772 1000

Cover: Artistic illustration of an interlayer exciton, composed of spatially separated electrons and holes, in a van der Waals heterostructure. The figure was generated using OpenAI and DALL-E 3.0.

Printed at Chalmers digitaltryck
Göteborg, Sweden 2023

Quantum Theory of Exciton-Exciton Interactions in Atomically Thin Semiconductors

Daniel Erkensten
Department of Physics
Chalmers University of Technology

Abstract

Atomically thin materials such as transition-metal dichalcogenides (TMDs) have emerged as an unprecedented platform for engineering future optoelectronic devices and studying exotic quantum phases of matter. In particular, the strong Coulomb interaction in these materials enables the formation of tightly-bound excitons, electron-hole pairs with neither purely fermionic nor bosonic character. These intriguing quasiparticles dominate the optical response, dynamics and transport properties of TMDs.

The aim of this thesis is to investigate the impact of exciton-exciton interactions on optics, relaxation dynamics and diffusion in 2D materials. Based on the density-matrix formalism, we develop equations of motion which are used to study intriguing and technologically relevant phenomena in the high-excitation regime where interexcitonic interactions dominate. We shed light on the fundamentally different interactions between intra- and interlayer excitons in TMD monolayers and bilayers, respectively. Exciton-exciton interactions in monolayers are governed by quantum-mechanical exchange interactions and interlayer excitons in heterobilayers interact predominantly via dipole-dipole repulsion. Furthermore, we demonstrate the crucial importance of optically-dark recombination channels in exciton-exciton annihilation and reveal the dominant role of dipole-dipole repulsion in interlayer exciton transport. Finally, we show that interactions between layer-hybridized excitons are electrically tunable and that electric fields can be used to boost and control the exciton propagation in van der Waals heterostructures. Our material-specific and predictive theory has allowed us to predict experimental observations, such as density-dependent exciton line-shifts and exciton-exciton annihilation rates, that have been verified through joint theory-experiment collaborations. Overall, this thesis provides microscopic insights into exciton-exciton interactions, which are expected to play a central role in the optimal operation of optoelectronic devices and the realization of strongly correlated electron-hole systems.

Keywords: transition-metal dichalcogenides, 2D materials, dark excitons

List of publications

This thesis contains an introductory text and the following appended papers:

I. **Exciton-exciton interaction in transition metal dichalcogenide monolayers and van der Waals heterostructures**
D. Erkensten, S. Brem, E. Malic
Physical Review B **103**, 045426 (2021)

II. **Dark exciton-exciton annihilation in monolayer WSe_2**
D. Erkensten, S. Brem, K. Wagner, R. Perea-Causin, R. Gillen, J.D. Ziegler, T. Taniguchi, K. Watanabe, J. Maultzsch, A. Chernikov, E. Malic
Physical Review B **104**, L241406 (2021) (Editor's Suggestion)

III. **Microscopic origin of anomalous interlayer exciton transport in van der Waals heterostructures**
D. Erkensten, S. Brem, R. Perea-Causin, E. Malic
Physical Review Materials **6**, 094006 (2022)

IV. **Electrically tunable dipolar interactions between layer-hybridized excitons**
D. Erkensten, R. Perea-Causin, S. Brem, J. Hagel, F. Tagarelli, E. Lopriore, A. Kis, E. Malic
Nanoscale **15**, 11064-11071 (2023)

V. **Electrical control of hybrid exciton transport in a van der Waals heterostructure**
F. Tagarelli, E. Lopriore, **D. Erkensten**, R. Perea-Causin, S. Brem, J. Hagel, Z. Sun, G. Pasquale, T. Taniguchi, K. Watanabe, E. Malic, A. Kis
Nature Photonics **17**, 615-621 (2023)

My contributions to the appended papers
As first-author in Papers I-IV, I developed the microscopic theory, performed the numerical calculations, analyzed the results and wrote the papers with input from my supervisor. In Paper V, I was the leading theory-author and I developed the microscopic theory and performed all simulations.

Publications not appended in thesis

VI. **Topology of critical chiral phases: Multiband insulators and superconductors**
O. Balabanov, **D. Erkensten**, H. Johannesson
Physical Review Research **3**, 043048 (2021)

VII. **Fermi-Pressure and Coulomb repulsion driven rapid hot plasma expansion in a van der Waals heterostructure**
J. Choi, J. Embley, D. Blach, R. Perea-Causin, **D. Erkensten**, S. Brem, D. Kim, L. Yuan, T. Taniguchi, K. Watanabe, K. Ueno, E. Tutuc, E. Malic, X. Li, and L. Huang
Nano Letters 23 (10), 4399-4405 (2023)

VIII. **Exciton optics, dynamics and transport in atomically thin semiconductors**
R. Perea-Causin, **D. Erkensten**, J. Fitzgerald, J. Thompson, R. Rosati, S. Brem, E. Malic
APL Materials 10 100701 (2022)

IX. **Interlayer exciton polaritons in homobilayers of transition metal dichalcogenides**
J. Köing, J. Fitzgerald, J. Hagel, **D. Erkensten**, E. Malic
2D Materials **10** 025019 (2023)

X. **Exciton transport in atomically thin semiconductors**
E. Malic, R. Perea-Causin, R. Rosati, **D. Erkensten**, S. Brem
Nature Communications, 14, 3430 (2023)

My contributions to the non-appended publications
In Paper VI, I set up the underlying theoretical framework and contributed in discussions. In Papers VII and IX, I took part in developing the theoretical model. Paper VIII is a review article in which I share the first-authorship with R. Perea-Causin. Paper X is a comment, where I contributed with writing of the manuscript.

Contents

1 Introduction

Two-dimensional (2D) materials have remained at the heart of materials science for more than a decade. In 2004, Andre Geim and Konstantin Novoselov successfully isolated and characterized a single layer of carbon atoms — graphene, a nanomaterial with exceptional optical, mechanical and electronic properties [1]. Their pioneering work on graphene spurred an immense interest in the rapidly growing family of atomically thin 2D materials, which today ranges from insulating hexagonal boron nitride to semiconducting or even superconducting transition-metal dichalcogenides (TMDs).[1] The latter have emerged as a highly promising class of materials for studying intriguing many-body phenomena and hold prospects for being integrated into the next-generation electronic and optoelectronic devices [3–7]. TMDs are composed by a transition metal (typically molybdenum or tungsten) sandwiched between two layers of chalcogens (typically selenium, sulfur or tellurium), as illustrated in Fig. 1.1. The semiconducting TMDs, including the extensively studied $MoSe_2$, MoS_2, WSe_2 and WS_2, exhibit weak dielectric screening due to their two-dimensional nature. Concretely, the electric field lines generated by the charge carriers confined in the TMD extend outside the material and into the surrounding environment, which typically has a smaller permittivity. As a consequence, the Coulomb interaction between charges inside

[1] The first transition-metal dichalcogenide monolayer was exfoliated in 2010 [2]. The very same year, Geim and Novoselov were awarded the Nobel Prize for their groundbreaking experiments on graphene.

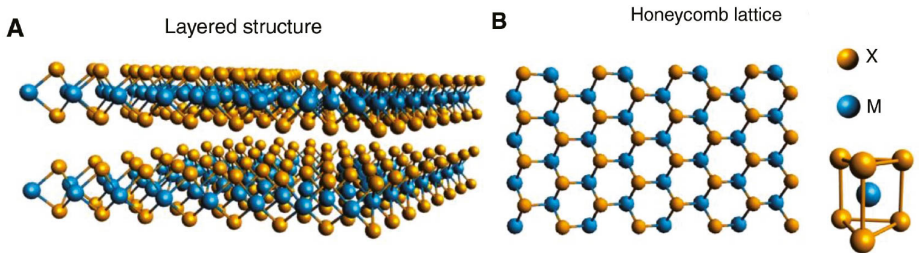

Figure 1.1: TMD monolayers have the chemical composition MX_2, where M is a transition metal and X is a chalcogen. The monolayers are shown from the side (A) and from the top (B), revealing their honeycomb structure. Figure adapted from [8] under a CCBY 4.0 license.

the TMD is remarkably strong and favors the formation of tightly-bound electron-hole pairs, i.e. excitons [9,10]. These quasi-particles exhibit binding energies of hundreds of meVs making them stable even at room temperature. Therefore, excitons are said to dominate the optical response of TMDs and are expected to govern the efficiency of TMD-based photodetectors and LEDs [7,11]. Obtaining a microscopic understanding of these quasi-particles and their interaction mechanisms is hence crucial.

In recent years, the scattering mechanisms of excitons with other quasi-particles including phonons [12–17], free or microcavity photons [18–20], free charges in the presence of doping [21,22], and their impact on exciton optics, dynamics and transport have received large attention. At elevated densities of electrons and holes, excitons scatter also efficiently with other excitons, which results in a broad range of interaction-driven phenomena including excitation-induced dephasing [23, 24], exciton-exciton annihilation [25, 26], density-dependent energy renormalizations of exciton resonances [27–30], and anomalous exciton transport [31–34]. Although all these phenomena have been experimentally observed, their microscopic origin have remained elusive in transition-metal dichalcogenides owing to the complex nature of the exciton-exciton interaction. In particular, excitons are typically formed via optical excitation and their scattering characteristics are determined by the exciton density. In the low-excitation regime, excitons behave as non-interacting bosons, but at higher densities their underlying fermionic sub-structure influences the scattering characteristics [35,36].

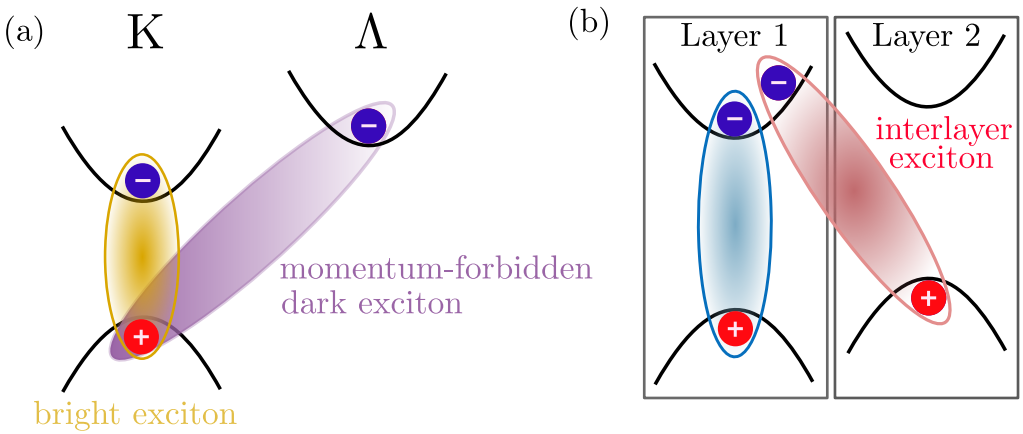

Figure 1.2: Exciton species in monolayer and bilayers with a parabolic band structure. (a) Bright KK excitons (yellow) and dark KΛ excitons (purple) in a TMD monolayer. (b) Intralayer (blue) and interlayer (red) excitons in a heterobilayer with type-II band alignment.

In addition, the complex band structure of TMDs containing multiple valleys and sizable spin-orbit coupling [37, 38] gives rise to a plethora of optically active (bright) and inactive (dark) exciton states and results in a large phase-space for scattering, see Fig. 1.2(a) [39]. The bright excitons form when electrons are promoted from the valence band to the conduction band at a single high-symmetry point in the hexagonal Brillouin zone. In contrast, (momentum)-dark excitons are composed by electrons and holes at different symmetry points in the Brillouin zone [39–41] and need to scatter with phonons in order to recombine [15, 42, 43]. There exists also spin-dark excitons, i.e. excitons where the electrons and holes reside in conduction and valence bands with opposite spin polarization. These excitons can recombine e.g. via chiral phonons or can be seen directly in certain photoluminescence experiments relying on a large aperture objective able to collect the radiation stemming from their small but finite out-of-plane optical dipole moments [14].

The ultrathin nature of transition-metal dichalcogenides allows for stacking TMD monolayers of top of each other, resulting in a van der Waals

heterostructure [44].[2] Importantly, this extends the exciton landscape to spatially separated interlayer excitons which are long-lived and exhibit out-of-plane dipole moments (cf. Fig. 1.2(b)). The intra- and interlayer excitons in a TMD multilayer can also be hybridized across the layers such that they have both an intralayer and an interlayer component due to significant carrier tunneling. The dipolar nature of interlayer or interlayer-like excitons allows these exciton species to couple efficiently to out-of-plane electric fields, which could make them useful in the realization of electrically controlled devices [50–53]. Finally, the long life-time of interlayer-like excitons could facilitate exciton condensation [3, 4, 54].

1.1 Outline

In this thesis, we aim to investigate the impact of exciton-exciton interactions on exciton optics, dynamics and transport in atomically thin semiconductors at the microscopic level. In Chapter 2, a brief introduction to the theoretical framework used throughout the thesis is given, i.e. the density-matrix formalism and second quantization. In particular, we here emphasize the Coulomb interaction and show how it gives rise to excitons. In addition, the versatile exciton landscape in transition-metal dichalcogenides is discussed. The electronic interactions and the relevant excitonic states are crucial inputs for the exciton-exciton interaction discussed in Chapter 3. We show how to formulate the exciton-exciton Hamiltonian and discuss the exciton-exciton interaction in the context of intralayer, interlayer, and layer-hybridized excitons, respectively. In Chapter 4, we demonstrate how exciton-exciton interactions lead to experimentally accessible density-dependent shifts of exciton resonances and in Chapter 5, we reveal the crucial role of dipole-dipole repulsion in interlayer and hybrid exciton transport. Furthermore, in Chapter 6, we shed light on exciton-exciton annihilation in TMD monolayers, a non-

[2] In fact, stacking single monolayer crystals at different angles initiated the exciting field of *twistronics*. This research field has gained immense attention recently, not the least since the remarkable discovery of superconductivity in twisted bilayer graphene in 2018 by Pablo Jarillo-Herrero and collaborators [45]. Besides superconductivity, many so-called moiré structures have been shown to host a plethora of intriguing correlated states of matter including generalized Wigner crystal states, exciton density waves, and Mott insulators [46–49].

radiative Auger-like recombination process which fundamentally limits quantum yields of 2D materials. Finally, in Chapter 7, some concluding remarks and intriguing prospects for future research are provided.

1.2 Key outcomes

The thesis is based on five papers (I-V) and the key outcomes of each paper are listed below.

Paper I: In this work we unveil the underlying mechanisms of exciton-exciton scattering in TMD monolayers and heterostructures. In particular, we find that intralayer excitons exhibit predominantly exchange interactions owing to their fermionic substructure whereas interlayer excitons interact via classical dipole-dipole repulsion. This paper served as a first step towards understanding exciton-exciton interactions. Additional contributions to the interaction including carrier-carrier exchange and correlation effects have been added in subsequent publications. The main findings of Paper I are discussed in Chapter 3.

Paper II: In this joint theory-experiment study, we reveal the crucial importance of dark excitons in exciton-exciton annihilation (EEA) in WSe_2 monolayers. We develop a general microscopic model for exciton-exciton annihilation and find a characteristic temperature dependence of the EEA rates, which is supported by temperature- and time-resolved photoluminescence measurements. The microscopic model and the insights of Paper II are summarized in Chapter 6.

Paper III: In this work, we investigate the role of dipole-dipole repulsion, exchange and correlation effects in interlayer exciton transport in $MoSe_2$-WSe_2 heterostructures. Based on the Wigner function formalism, we find that dipole-dipole repulsion between interlayer excitons accelerates the exciton transport at elevated densities and renders the linear diffusion to anomalous diffusion. The exciton transport is, however, slowed down by attractive exchange interactions and significant screening from surrounding excitons. The impact of exchange and correlations contributions on exciton optics is discussed in Chapter 4 and section 4.1. Interlayer exciton transport is discussed

in Chapter 5, sections 5.1-5.2.

Paper IV-V: In both these works, we reveal the remarkable electrical tunability of hybrid excitons and how exciton transport can be electrically controlled in WSe_2 homobilayers. In **Paper IV**, we microscopically model hybrid exciton-exciton interactions and reveal the emergence of two interaction regimes involving mostly intralayer-like and interlayer-like excitons, at low and high electric fields, respectively. In the joint experiment-theory study, **Paper V**, the theoretically predicted interaction regimes are also verified experimentally by means of spatiotemporally resolved photoluminescence measurements and shown to result in highly electric-field-dependent exciton transport. The electrical tuning of hybrid exciton-exciton interactions is discussed in Sections 3.4 and 4.2. Hybrid exciton transport is discussed in Chapter 5, section 5.3.

2

Theoretical framework

Here, a brief introduction to the theoretical framework used to model many-body interactions in two-dimensional semiconductors is provided. The framework relies on second quantization, a formalism which in the field of condensed matter physics is commonly used to model the excitation kinetics of a quantum system of interacting electrons, phonons and photons. Here, we focus on the electronic interaction mechanisms of relevance to this work and the appended papers, i.e. the Coulomb interaction between carriers. In particular, we show how the strong Coulomb interaction in two-dimensional materials gives rise to tightly bound excitons.

2.1 Second quantization formalism

In quantum mechanics, we usually distinguish between two different types of particles: bosons and fermions. The distinction originates from the symmetry of wave functions under particle exchange, with the wave function being symmetric for bosons and anti-symmetric for fermions. The former can in second quantization formalism be represented by commuting creation operators $b_i^\dagger$ (or annihilation operators b_i) and the latter are represented by

anti-commuting operators $a_i^{(\dagger)}$ such that

$$\begin{aligned} \{a_i, a_j^\dagger\} &= \delta_{i,j} \quad \text{(fermions)} \\ [b_i, b_j^\dagger] &= \delta_{i,j} \quad \text{(bosons)} \ , \end{aligned} \tag{2.1}$$

where the compound indices i, j contain information about the state of the particles, e.g. their momentum, spin, band and valley they reside in[1]. Typical examples of bosons are phonons or photons and common fermions are electrons or holes (signifying a vacancy in the valence band, i.e. the absence of an electron). Depending on the density also excitons, although formally being a combination of electrons and holes, can be described as non-interacting bosons [55–57]. This topic will be further discussed in Chapter 3. Here, we only consider interactions between fermions.

Using second quantization formalism we may connect the creation and annihilation operators introduced above to single- and two-particle operators, $\hat{O}_1$ and $\hat{O}_2$, respectively. In particular, single-particle operators only involve the coordinates of a single particle, and two-particle operators, such as the Coulomb interaction between charges, involve coordinates of two particles. The operators are generally expressed as

$$\hat{O}_1 = \sum_{i,j} \langle i|\hat{o}_1|j\rangle a_i^\dagger a_j \ , \hat{O}_2 = \frac{1}{2} \sum_{i,j,l,m} \langle i,j|\hat{o}_2|l,m\rangle a_i^\dagger a_j^\dagger a_l a_m \ , \tag{2.2}$$

where the first-quantized operators $\hat{o}_1$ and $\hat{o}_2$ act on single particle states $|i\rangle$ and two-particle states $|i,j\rangle$, respectively. The expressions in Eq. (2.2) also hold for bosons. Most many-body systems can be described by a Hamiltonian operator, $\hat{H} = \sum_i \hat{O}_1^i + \sum_i \hat{O}_2^i$, which is given by the sum of single-particle and two-particle contributions. In the following, we will present the many-particle Hamiltonian of relevance to this work.

[1]The word valley in the context of intra- and intervalley excitons is used extensively in this thesis. The electronic band structure of transition-metal dichalcogenides exhibits multiple valleys in the first Brillouin zone, that is, local extrema, in which it is energetically favorable for a particle to reside in.

2.2 Many-particle Hamiltonian

The Hamiltonian is a crucial quantity which determines the energy spectrum and the time evolution of a quantum system. Here, the quantum system we consider includes interacting and photo-excited electrons in a two-dimensional lattice. In particular, such a system is described by the electronic many-particle Hamiltonian $H = H_0 + H_{\mathrm{c-c}}$ where H_0 is the kinetic contribution due to (quasi)-free electrons in a lattice and $H_{\mathrm{c-c}}$ is the electron-electron Hamiltonian.[2]

Kinetic Hamiltonian

The Hamiltonian describing (quasi)-free electrons in a lattice reads

$$H_0 = \sum_{\lambda,\mathbf{k}} \epsilon^{\lambda}_{\mathbf{k}} a^{\dagger}_{\lambda,\mathbf{k}} a_{\lambda,\mathbf{k}} \ , \tag{2.3}$$

with the single-particle band structure $\epsilon^{\lambda}_{\mathbf{k}}$ being dependent on momentum or wave number $\mathbf{k}$ and the band index λ. The electronic band structure is typically obtained from *ab initio* calculations and contains several conduction band minima or valence band maxima around the symmetry points of the Brillouin zone. In Fig. 2.1, we show the schematic band structure of a transition-metal dichalcogenide monolayer revealing a direct band gap at the K-point. In particular, we note that optical excitation takes place around the $\mathrm{K}^{(')}$-points, but that also the Γ and $\Lambda^{(')}$-points[3] could be important for scattering processes involving holes and electrons, respectively. Moreover, the K and K'-valleys and the Λ and Λ'-valleys have opposite spin configuration and are related by time-reversal symmetry [37]. The ordering of spin-split bands (red and blue lines) in the band structure corresponds to a tungsten-based material, while in molybdenum-based TMDs the two conduction bands are swapped [38]. See e.g. Ref. [38] for more details on the band structures of TMDs. Around the symmetry points the single-particle dispersion can be

[2] More generally, the Hamiltonian contains contributions also from other quasiparticles such as phonons and photons. We will focus on the electronic contributions here.

[3] The Λ-point is also commonly denoted the Q-point or Σ-point in literature.

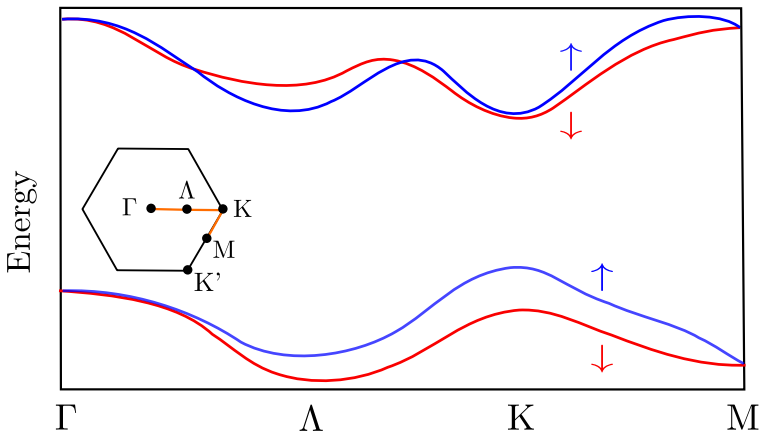

Figure 2.1: Sketch of band structure of a W-based transition-metal dichalcogenide monolayer. The band structure is shown along the $\Gamma - \Lambda - \mathrm{K} - \mathrm{M}$ line in the hexagonal Brillouin zone (inset) and includes spin-orbit split bands (red and blue lines).

approximated as a parabola within the effective mass approximation [58]

$$\epsilon_{\mathbf{k}}^{\lambda} = \epsilon_0^{\lambda} + \frac{\hbar^2 k^2}{2m^{\lambda}} \ , \tag{2.4}$$

where $\lambda = c$ ($\lambda = v$), is a conduction band (valence band), and ϵ_0^{λ} is a constant energy taking into account e.g. spin-orbit splitting of bands (red and blue lines in Fig. 2.1). The momentum $\mathbf{k}$ is expressed relative to the considered high-symmetry point in the Brillouin zone and m^{λ} is the effective mass. The effective mass is directly related to the (inverse) curvature of the band such that $m^{\lambda} = \hbar^2/\partial_k^2 \epsilon_{\mathbf{k}}^{\lambda}$, and is directly extracted from the single-particle band structure.

Electron-electron Hamiltonian

Now, we consider the interaction between charge carriers represented by the following two-particle Hamiltonian

$$H_{\mathrm{c-c}} = \frac{1}{2} \sum_{i,j,l,m} V^{ijlm} a_i^{\dagger} a_j^{\dagger} a_l a_m \ , \tag{2.5}$$

where $V^{ijlm} = \langle i,j|V(\mathbf{r}-\mathbf{r}')|l,m\rangle$ is the Coulomb matrix element and can be expressed via the Fourier transform as

$$V^{ijlm} = \sum_{\mathbf{q}} V_{\mathbf{q}} F_{im}(\mathbf{q}) F_{jl}(-\mathbf{q}) \ , F_{fi}(\mathbf{q}) = \langle f|\mathrm{e}^{i\mathbf{q}\cdot\mathbf{r}}|i\rangle \ , \tag{2.6}$$

where the form-factor $F_{fi}(\mathbf{q})$ describes the probability of scattering from an initial state $|i\rangle$ to a final state $|f\rangle$ with the momentum transfer $\mathbf{q}$. The Coulomb interaction includes intraband ($\lambda_i = \lambda_m = \lambda_j = \lambda_l$) as well as interband processes, i.e. scattering processes involving different bands. By restricting to the dominant scattering processes with a small momentum transfer $\mathbf{q}$ (compared to the Brillouin zone) we may approximate the form-factors as

$$F_{fi}(\mathbf{q}) = \langle \mathbf{k}_f, \lambda_f|\mathrm{e}^{i\mathbf{q}\cdot\mathbf{r}}|\mathbf{k}_i, \lambda_i\rangle \approx \delta_{\lambda_i,\lambda_f}\delta_{\mathbf{q},\mathbf{k}_f-\mathbf{k}_i} + i\mathbf{q}\cdot\mathbf{d}_{\lambda_f\lambda_i} \ , \tag{2.7}$$

where we have here assumed Bloch states as initial and final states, i.e. $\langle \mathbf{r}|i\rangle = \mathrm{e}^{i\mathbf{k}_i\cdot\mathbf{r}} u_{\lambda_i\mathbf{k}_i}(\mathbf{r})$ and introduced the transition dipole matrix element $\mathbf{d}_{\lambda_f\lambda_i} = \langle \mathbf{k}_f, \lambda_f|\mathbf{r}|\mathbf{k}_i, \lambda_i\rangle$. The transition dipole matrix element can also be expressed in terms of an optical matrix element, $\mathbf{M}_{\lambda_f\lambda_i} = \langle \mathbf{k}_f, \lambda_f|\nabla_{\mathbf{k}}|\mathbf{k}_i, \lambda_i\rangle \propto \mathbf{d}_{\lambda_f\lambda_i}$ [59]. Furthermore, we consider in the following a two-band model including one conduction band c and one valence band v ($\lambda = c,v$). In this specific case we may express the Coulomb interaction as

$$\begin{aligned} H_{c-c} = &\frac{1}{2}\sum_{\substack{\mathbf{k},\mathbf{k}',\mathbf{q}\\ \lambda,\lambda'}} V_{\mathbf{q}}^{\lambda\lambda'} a^{\dagger}_{\lambda,\mathbf{k}+\mathbf{q}} a^{\dagger}_{\lambda',\mathbf{k}'-\mathbf{q}} a_{\lambda',\mathbf{k}'} a_{\lambda,\mathbf{k}} \\ &+ \frac{1}{2}\sum_{\substack{\mathbf{k},\mathbf{k}',\mathbf{q}\\ \lambda\neq\lambda'}} \bar{V}_{\mathbf{q}}^{\lambda\lambda'} a^{\dagger}_{\lambda,\mathbf{k}+\mathbf{q}} a^{\dagger}_{\lambda',\mathbf{k}'-\mathbf{q}} a_{\lambda,\mathbf{k}'} a_{\lambda',\mathbf{k}} \ , \end{aligned} \tag{2.8}$$

with $V_{\mathbf{q}}^{\lambda\lambda'} = V_{\mathbf{q}}$ and $\bar{V}_{\mathbf{q}}^{\lambda\lambda'} \equiv V_{\mathbf{q}}|\mathbf{q}\cdot\mathbf{M}_{\lambda\lambda'}|^2$ making use of Eq. (2.7). The second interband term in Eq. (2.8) is commonly referred to as the electron-hole exchange interaction [60]. In Fig. 2.2, we provide a schematic illustration of the relevant intraband and interband Coulomb scattering processes within the parabolic two-band model. Here, we have excluded terms with an odd number of conduction band or valence band electron operators, i.e. terms describing Auger or impact excitation processes [61, 62]. Auger recombination is discussed in detail in Chapter 6. Up to this point, we have only discussed the Coulomb interaction for an ideal many-body system. In order to

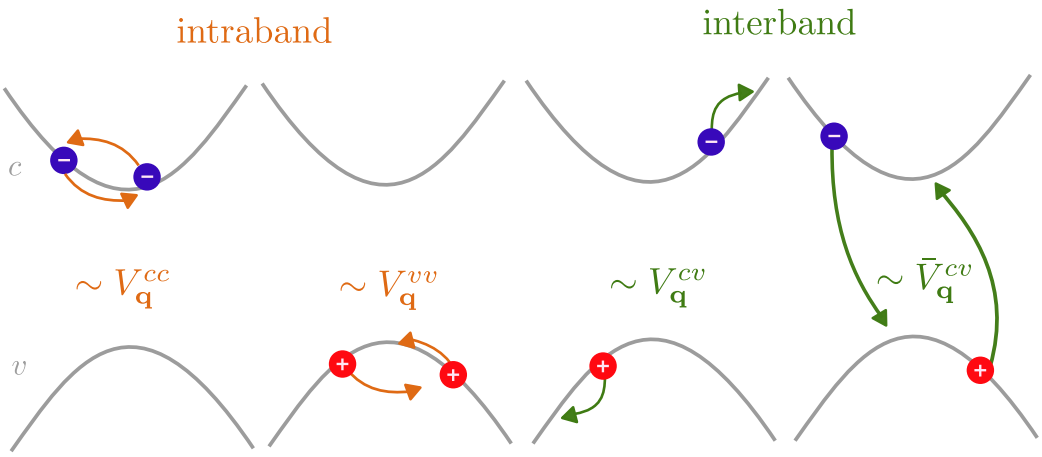

Figure 2.2: Schematic illustration of intraband and interband Coulomb scattering processes for a two-band model with parabolic bands.

develop a material-specific model which accurately captures interactions between charges inside a real semiconductor, we also have to take into account finite thickness effects as well as the screening from substrates/environment. Therefore, for two-dimensional semiconductors we employ the widely used Keldysh-like screening [63–66] and consider a screened Coulomb potential

$$V_{\mathbf{q}} = \frac{V_{\text{bare},\mathbf{q}}}{\varepsilon_{\mathbf{q}}} \, , V_{\text{bare},\mathbf{q}} = \frac{e_0^2}{2\epsilon_0 A|\mathbf{q}|} \, , \tag{2.9}$$

where A is the crystal area, e_0 is the electric charge, ϵ_0 is the vacuum permittivity and $\varepsilon_{\mathbf{q}}$ is the dielectric screening. For TMD monolayers[4] the screening is described within a Rytova-Keldysh framework [63, 64] and given by the dielectric function [15]:

$$\varepsilon_{\mathbf{q}} = \kappa_{\text{TMD}} \tanh\left[\frac{1}{2}[\alpha_{\text{TMD}} dq - \ln(\frac{\kappa_{\text{TMD}} - \kappa_{\text{sub}}}{\kappa_{\text{TMD}} + \kappa_{\text{sub}}})]\right] \, , \tag{2.10}$$

where d is the layer thickness of the TMD, $\kappa_{\text{TMD}} = \sqrt{\varepsilon^{||}\varepsilon^{\perp}}$, $\alpha_{\text{TMD}} = \sqrt{\varepsilon^{||}/\varepsilon^{\perp}}$, $\varepsilon^{||}$ and $\varepsilon^{\perp}$ being the in-plane and out-of-plane components of the dielectric tensor of the TMD respectively and κ_{sub} is the effective dielectric constant

[4] In Papers I, III, IV-V we also considered TMD monolayers stacked on top of each other, i.e. van der Waals heterostructures. In this case the Keldysh screening has to be modified, which is done by solving the Poisson equation for a multilayer system [51, 67].

of the substrate, here assumed to be given by the average of the dielectric constants above and below the semiconductor. The material-specific dielectric constants are extracted from *ab initio* calculations [68, 69]. A linearized version of (2.10) is also commonly used in literature which holds assuming $dq \ll 1$ and $\kappa_{\text{sub}} \ll \kappa_{\text{TMD}}$, $\varepsilon_{\mathbf{q}} = \kappa_{\text{sub}} + \frac{d\varepsilon^{||}q}{2}$. When describing scattering processes involving a large momentum transfer (of the order of a reciprocal lattice vector, $\mathbf{G}$) one has to extract the screening from *ab initio* calculations or consider a more refined screening model than the one provided by (2.10).[5]

2.3 Heisenberg's equation of motion

Equipped with the electronic Hamiltonian including the relevant interaction mechanisms, we are able to investigate how the many-body system evolves in time and obtain microscopic access to observables using the Heisenberg equation of motion. In the Heisenberg picture of quantum mechanics, observables are defined as expectation values of time-dependent operators and their time evolution is governed by the equation of motion

$$i\hbar \frac{d}{dt}\langle A \rangle = \langle [A, H] \rangle \ , \tag{2.11}$$

where A is the operator of interest, here assumed to be explicitly time-independent. In principle, A can be expressed as any combination of bosonic and fermionic creation and annihilation operators, but in practice we are interested in the time evolution of physically relevant quantities such as microscopic polarizations $p_{\mathbf{k},\mathbf{k}'} = \langle a^\dagger_{c,\mathbf{k}} a_{v,\mathbf{k}'} \rangle$, describing a single electronic transition from the valence band to the conduction band, or band occupations $f^\lambda_{\mathbf{k}} = \langle a^\dagger_{\lambda,\mathbf{k}} a_{\lambda,\mathbf{k}} \rangle$. More generally, the microscopic polarization and the occupations are off-diagonal and diagonal elements of a density matrix respectively, and the common framework in which these quantities are dealt with is referred to as the density matrix formalism. Additional details on the formalism can be found in [72]. Here, we focus on the equation of motion for the polarization. By making use of Eq. (2.8) (here focusing on the first term

[5] In Paper II, we considered such exciton scattering processes and therefore we adapted an analytic screening model [66] which is in good agreement with *ab initio* calculations [70, 71] also in the short wave-length limit.

in Eq. (2.8)) we find

$$\dot{p}_{\mathbf{k},\mathbf{k}'} = \frac{i}{\hbar}(\epsilon^c_{\mathbf{k}} - \epsilon^v_{\mathbf{k}'})p_{\mathbf{k},\mathbf{k}'} \\ - \frac{i}{\hbar}\sum_{\substack{\mathbf{k}_1,\mathbf{q},\\ \lambda}}(V^{v\lambda}_{\mathbf{q}}\langle a^\dagger_{c,\mathbf{k}}a^\dagger_{\lambda,\mathbf{k}_1-\mathbf{q}}a_{\lambda,\mathbf{k}_1}a_{v,\mathbf{k}'-\mathbf{q}}\rangle + V^{\lambda c}_{\mathbf{q}}\langle a^\dagger_{\lambda,\mathbf{k}_1+\mathbf{q}}a^\dagger_{c,\mathbf{k}-\mathbf{q}}a_{\lambda,\mathbf{k}_1}a_{v,\mathbf{k}'}\rangle) \ . \tag{2.12}$$

Now, we have encountered a typical problem when dealing with Heisenberg equations of motion and many-particle interactions: the single-particle quantity ($\sim \langle a^\dagger_i a_j\rangle$) in the left-hand side of the equation couples to a two-particle quantity ($\sim \langle a^\dagger_i a^\dagger_j a_l a_m\rangle$), which in turn needs to be evaluated, leading to a system of differential equations which is not closed. This issue is referred to as the hierarchy problem and is solved by applying a cluster expansion and systematic truncation. In general, any many-particle operator quantity can be factorized into correlations denoted by $\langle ...\rangle^c$ of lower order [72]. Here, we will only provide the important cluster expansion for a fermionic two-particle expectation value, the so-called Hartree-Fock factorization:[6]

$$\langle a^\dagger_i a^\dagger_j a_k a_l\rangle = \langle a^\dagger_j a_k\rangle\langle a^\dagger_i a_l\rangle - \langle a^\dagger_j a_l\rangle\langle a^\dagger_i a_k\rangle + \langle a^\dagger_i a^\dagger_j a_k a_l\rangle^c \ . \tag{2.13}$$

The theory is now said to be treated on a Hartree-Fock level or a mean-field level, which simplifies the system to a single-particle problem in which the many-body correlations $\langle ...\rangle^c$ are dropped. However, in order to describe scattering processes such as carrier-carrier scattering or exciton-exciton scattering (cf. Paper I) or the formation of bound particles, the correlations have to be kept. Here, we apply the Hartree-Fock approximation (2.13) to Eq. (2.12) and deduce

$$\dot{p}_{\mathbf{k},\mathbf{k}'} = \frac{i}{\hbar}(\tilde{\epsilon}^c_{\mathbf{k}} - \tilde{\epsilon}^v_{\mathbf{k}'})p_{\mathbf{k},\mathbf{k}'} - \frac{i}{\hbar}(f^v_{\mathbf{k}'} - f^c_{\mathbf{k}})\sum_{\mathbf{q}} V^{cv}_{\mathbf{q}}p_{\mathbf{k}+\mathbf{q},\mathbf{k}'+\mathbf{q}} \ , \tag{2.14}$$

with the renormalized band energies

$$\tilde{\epsilon}^\lambda_{\mathbf{k}} = \epsilon^\lambda_{\mathbf{k}} - \sum_{\mathbf{q}} V^{\lambda\lambda}_{\mathbf{q}}f^\lambda_{\mathbf{k}+\mathbf{q}} \ . \tag{2.15}$$

[6] A similar expansion can be made for bosonic operators, $b^{(\dagger)}_i$, but then the intermediate minus sign becomes a plus sign, reflecting their commuting nature.

Noting that the occupation of valence band electrons $f^v_{\mathbf{k}} = 1 - f^h_{\mathbf{k}}$, where $f^h_{\mathbf{k}}$ is the occupation of holes, we can rewrite the equations above in terms of electrons and holes and obtain the semiconductor Bloch equation for the polarization in the absence of electron-light coupling [72]. In the low excitation regime, it furthermore holds that $f^v_{\mathbf{k}} \approx 1$ and $f^c_{\mathbf{k}} \approx 0$ which simplifies the equations drastically. However, when treating exciton-exciton interactions which become important at high electron-hole densities, the phase-space filling factors ($\sim f^v, f^c$) should be kept, as discussed in detail in Section 4.1. Let us now consider (2.14) in detail, in this chapter assuming low densities of electrons and holes. The presence of the second term, which is due to the electron-hole interactions gives, as we shall see, rise to excitons.

2.4 The emergence of excitons

We shall now show that the electron-hole interaction results in bound excitons, quasiparticles whose binding energy is governed by the Coulomb interaction. Assuming small densities of electrons and holes, the eigenfrequency of the polarization is given by the transition energy $\epsilon^c_{\mathbf{k}} - \epsilon^v_{\mathbf{k}'}$ (up to a factor $\hbar$), but the presence of the electron-hole Coulomb interaction leads to a mixing of electron and hole momenta. The mixing of electronic momenta can, however, be disentangled by going to a different basis. This can be easily achieved by transforming the electronic momenta $\mathbf{k}, \mathbf{k}'$ to the center-of-mass momentum $\mathbf{Q}$ and relative momentum $\mathbf{q}$ defined according to

$$\mathbf{Q} = \mathbf{k} - \mathbf{k}' \ , \mathbf{q} = \beta\mathbf{k} + \alpha\mathbf{k}' \ , \tag{2.16}$$

introducing the mass ratios $\beta = m_h/(m_e + m_h)$ and $\alpha = m_e/(m_e + m_h)$. Secondly, note that, in the vicinity of band extrema, the electronic dispersion can be well approximated by a parabolic dispersion (Eq. (2.4)) such that

$$\epsilon^c_{\mathbf{k}} - \epsilon^v_{\mathbf{k}'} = \frac{\hbar^2 k^2}{2m_e} + \frac{\hbar^2 k'^2}{2m_h} + E_g = \frac{\hbar^2 Q^2}{2M} + \frac{\hbar^2 q^2}{2\mu} + E_g \ , \tag{2.17}$$

where $M = m_e + m_h$ and $\mu = m_e m_h/(m_e + m_h)$ is the total and reduced mass of an electron-hole pair respectively and $E_g = \epsilon^c_0 - \epsilon^v_0$ is the quasiparticle band gap. Importantly, the center-of-mass and relative motion has been

decoupled through the effective mass approximation. Hence, we may project our microscopic polarization $p_{\mathbf{k},\mathbf{k}'}$ to an excitonic basis such that

$$p_{\mathbf{k},\mathbf{k}'} \rightarrow p_{\mathbf{q},\mathbf{Q}} = \sum_n \varphi^*_{n,\mathbf{q}} P_{n,\mathbf{Q}} \ , \tag{2.18}$$

defining the orthonormal excitonic wave functions $\varphi_{n,\mathbf{q}}$, n numbering the excitonic state, and $P_{n,\mathbf{Q}}$ being the excitonic polarization. With these definitions and taking the low density limit (2.14) transforms into

$$\dot{P}_{n,\mathbf{Q}} = \frac{i}{\hbar}(\frac{\hbar^2 Q^2}{2M} + E_g + E_n) P_{n,\mathbf{Q}} \ , \tag{2.19}$$

where the eigenenergies E_n and associated eigenfunctions are obtained from the Wannier equation

$$\frac{\hbar^2 q^2}{2\mu}\varphi_{n,\mathbf{q}} - \sum_{\mathbf{k}} V^{cv}_{\mathbf{k}} \varphi_{n,\mathbf{k}+\mathbf{q}} = E_n \varphi_{n,\mathbf{q}} \ . \tag{2.20}$$

Now, we admire the simplicity of the equation above. We have just obtained an equation describing Wannier[7] excitons which is in perfect analogy to the corresponding time-independent Schrödinger equation for a hydrogen atom. Here, the attractive electron-hole interaction gives rise to strongly bound excitons. Similarly, as in the hydrogenic case, the energy levels of excitons follow a Rydberg-like series, $n = 1s,2p,2s...$, up to the continuum, as is schematically shown in Fig. 2.3 (b). However, importantly, in contrast to free hydrogen atoms, excitons in two-dimensional semiconductors are screened by its environment, that is by the TMD itself and its substrate. This crucially impacts the strength of the Coulomb interaction, through the non-local dielectric screening $\varepsilon_{\mathbf{q}}$, cf. (2.10). Furthermore, as already discussed in the previous chapter, the electrons and holes do not have to reside at the same high-symmetry point in the Brillouin zone, but can form so-called (momentum)-dark or intervalley excitons through the scattering with phonons [76,77]. Remarkably, even though the Λ-point lies above the K-point in the electronic band structure in tungsten-based TMDs (Fig. 2.3(a)), the

[7]Formally, one distinguishes between Wannier excitons [73], which are excitons with a Bohr radius (spatial extension) larger than the lattice spacing as is typically the case in semiconductors, and Frenkel excitons [74] which extend over a unit cell, typically found in molecular crystals [75]. Edward Frenkel invented the concept of excitons in 1931.

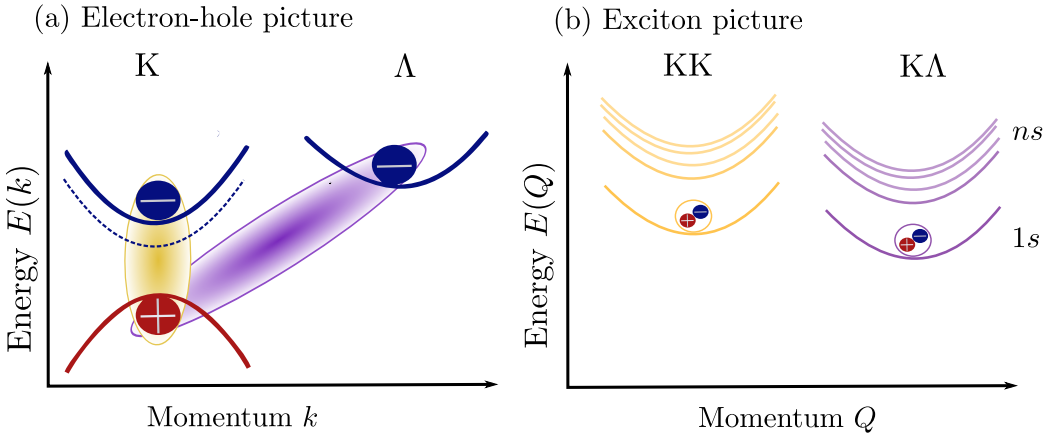

Figure 2.3: Excitons in the electron-hole picture and the excitonic picture for a W-based TMD monolayer. (a) Electrons and holes residing around the same high-symmetry point (K) form intravalley KK excitons (yellow). Electrons and holes may also form e.g. KΛ intervalley excitons (purple). The spin polarizations of the bands are indicated by solid and dashed lines respectively, and here we only consider spin-allowed, so-called A excitons. (b) In the excitonic picture, excitons exhibit a parabolic dispersion and form a Rydberg-like series of exciton states.

excitonic dark KΛ state lies energetically below the bright state in the exciton picture (Fig. 2.3(b)), due to the large electron mass at the Λ-point.

By numerically solving the eigenvalue problem in (2.20) employing the screening-dependent electron-hole interaction (2.9) with material-specific parameters obtained from *ab initio* calculations (including effective masses [38] and dielectric constants [68]), we get access to the energy spectrum of excitons.

In Fig. 2.4(a), we illustrate the $1s$ and $2p$ KK excitonic wave functions in monolayer WSe_2 encapsulated in the commonly used substrate hexagonal boron nitride (hBN), revealing the usual radial shape of s and p-states. As shown in Fig. 2.4 (b), the excitonic binding energies in TMDs are several hundreds of meV, and are significantly reduced when increasing the dielectric constant of the substrate. The huge binding energies found in TMDs enable excitons to be stable even at room temperature.

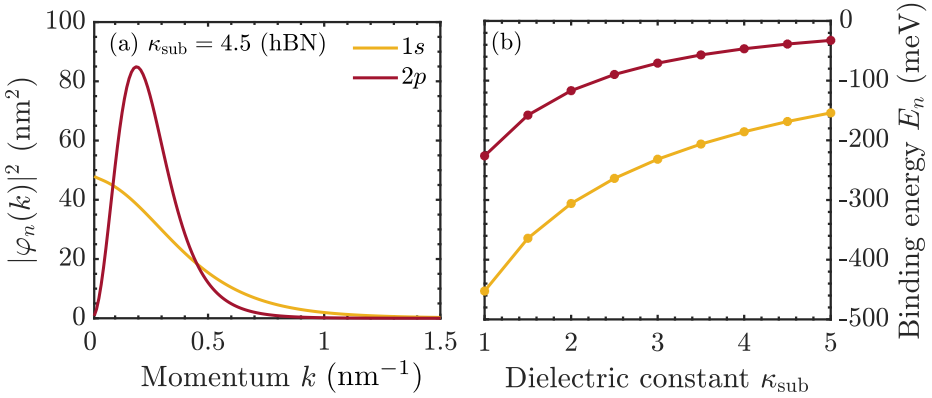

Figure 2.4: Wave functions and binding energies of KK excitons. (a): Excitonic wave functions for KK 1s and 2p excitons in hBN-encapsulated monolayer WSe_2. (b): Excitonic binding energies as function of the dielectric constant.

2.5 Excitonic operators

In the previous section we provided a general recipe for how excitonic effects can be accounted for in a microscopic theory. Firstly, we investigated the relevant interactions in the electron-hole picture and secondly, we found the equation of motion for an observable of our interest (e.g. the microscopic polarization or the carrier population) by means of Heisenberg's equation of motion and finally, we transformed the resulting equations of motion into an excitonic basis. An alternative approach to excitons relies on starting from a Hamiltonian which contains the excitonic effects from the beginning, i.e. a so-called excitonic Hamiltonian which is expressed through excitonic operators. This approach is highly convenient when it comes to treating interactions as it drastically reduces the number of operators needed to describe the dynamics. We will only sketch the derivation of the excitonic Hamiltonian[8] here and refer the interested reader to the works by Katsch *et al.* [55] in the context of excitons and Ivanov and Haug [56] for a more general treatment. Note that we may represent the creation and annihilation of an exciton with

[8]Historically, the excitonic Hamiltonian was first introduced through the boson formalism by Usui in 1960 [57] shortly followed by works from Marumori [78] and Hanamura [79]. However, here we employ the unit operator technique introduced by Ivanov and Haug in 1993 [56] and outlined in detail in [55].

the pair operators

$$P^{\dagger}_{\mathbf{k}_1,\mathbf{k}_2} = a^{\dagger}_{c,\mathbf{k}_1} a_{v,\mathbf{k}_2} \ , P_{\mathbf{k}_1,\mathbf{k}_2} = a^{\dagger}_{v,\mathbf{k}_2} a_{c,\mathbf{k}_1} \ , \tag{2.21}$$

respectively. Here, the pair operators are only dependent on the momenta $\mathbf{k}_1$ and $\mathbf{k}_2$, but they could also generally depend on valley, spin and layer configuration. In particular, the excitonic operator formalism can straightforwardly be extended to layer-hybridized excitons in TMD multilayers cf. Ref. [80] and Paper IV-V. Given the construction of the pair operators, the corresponding commutator relations are found directly using Eq. (2.1)

$$[P_{\mathbf{k}_1,\mathbf{k}_2}, P_{\mathbf{k}_3,\mathbf{k}_4}] = [P^{\dagger}_{\mathbf{k}_1,\mathbf{k}_2}, P^{\dagger}_{\mathbf{k}_3,\mathbf{k}_4}] = 0 \ , \tag{2.22}$$

and

$$[P_{\mathbf{k}_1,\mathbf{k}_2}, P^{\dagger}_{\mathbf{k}_3,\mathbf{k}_4}] = \delta_{\mathbf{k}_2,\mathbf{k}_4}\delta_{\mathbf{k}_1,\mathbf{k}_3} - \delta_{\mathbf{k}_2,\mathbf{k}_4} a^{\dagger}_{c,\mathbf{k}_3} a_{c,\mathbf{k}_1} - \delta_{\mathbf{k}_1,\mathbf{k}_3} a_{v,\mathbf{k}_2} a^{\dagger}_{v,\mathbf{k}_4} \ . \tag{2.23}$$

From the two equations above we obtain two crucial insights about excitons. First, we note that (2.22) states that two electron-hole pair annihilation or creation operators are symmetric under exchange. Secondly, (2.23) illustrates that excitons, in general, are neither bosons or fermions but obey so-called cobosonic commutator relations. In the weak excitation regime, in which the two-operator quantities $\langle a^{\dagger}_{c,\mathbf{k}_3} a_{c,\mathbf{k}_1} \rangle \sim f^c$ and $\langle a_{v,\mathbf{k}_2} a^{\dagger}_{v,\mathbf{k}_4} \rangle \sim f^h$ can be neglected, excitons can be directly approximated as bosons. However, excitons are composed of fermions and at elevated densities of electrons and holes, the commutator acquires correction terms of the order $\mathcal{O}(n_x a_{\mathrm{B}}^2)$ and beyond, n_x being the exciton density and a_{B} being the excitonic Bohr radius ($a_{\mathrm{B}} \sim 1$ nm, in the case of monolayer TMDs). As a consequence, one finds that excitons can be considered as weakly interacting bosons at densities $n_x \ll 10^{14}$ cm^{-2}.[9]

By employing the identity operator method [56] purely electronic quantities are transformed to the pair-operator picture as follows [55]

$$a^{\dagger}_{c,\mathbf{k}_1} a_{c,\mathbf{k}_2} \approx \sum_{\mathbf{k}_3} P^{\dagger}_{\mathbf{k}_1,\mathbf{k}_3} P_{\mathbf{k}_2,\mathbf{k}_3} - \frac{1}{2} \sum_{\mathbf{k}_3,\mathbf{k}_4,\mathbf{k}_5} P^{\dagger}_{\mathbf{k}_1,\mathbf{k}_3} P^{\dagger}_{\mathbf{k}_4,\mathbf{k}_5} P_{\mathbf{k}_4,\mathbf{k}_5} P_{\mathbf{k}_2,\mathbf{k}_3} \ , \tag{2.24}$$

[9] This crude density constraint does not take into account that the exciton Bohr radius also gets renormalized at elevated densities. Furthermore, at large densities of electrons and holes (typically at densities $n_x \sim 10^{13}$ cm^{-2} [81]), excitons undergo the so-called Mott transition, at which they dissociate into free electrons and holes. In this work, and throughout the appended papers we stay in a density regime well below the Mott transition.

and

$$a_{v,\mathbf{k}_1}a^\dagger_{v,\mathbf{k}_2} \approx \sum_{\mathbf{k}_3} P^\dagger_{\mathbf{k}_3,\mathbf{k}_1}P_{\mathbf{k}_3,\mathbf{k}_2} - \frac{1}{2}\sum_{\mathbf{k}_3,\mathbf{k}_4,\mathbf{k}_5} P^\dagger_{\mathbf{k}_3,\mathbf{k}_1}P^\dagger_{\mathbf{k}_4,\mathbf{k}_5}P_{\mathbf{k}_4,\mathbf{k}_5}P_{\mathbf{k}_3,\mathbf{k}_2} \ . \tag{2.25}$$

Formally, one has to include an infinite number of pair operator terms in the expansions above, but depending on the excitation regime it is often sufficient to just consider terms up to first order in the excitation density, such that f^e,$f^h \sim \langle P^\dagger P\rangle$. Additionally, we may, by analogy with (2.18), expand the pair operators in a complete set of excitonic wave functions and form new excitonic operators $X^{(\dagger)}$ according to

$$P^\dagger_{\mathbf{k}_1,\mathbf{k}_2} = \sum_n X^\dagger_{n,\mathbf{k}_1-\mathbf{k}_2}\varphi^*_{n,\beta\mathbf{k}_1+\alpha\mathbf{k}_2} \ , \tag{2.26}$$

where the sum is taken over all exciton states, $n = 1s$,$2p$,$2s$.... Now, taking the two-band Hamiltonian, $H = H_0 + H_{e-h}$ where H_0 is the free Hamiltonian (2.3) in the effective mass approximation and H_{e-h} contains the attractive electron-hole interaction, as an example, it can be transformed directly to an excitonic Hamiltonian via the pair operator expansions above:

$$\begin{aligned} H_0 &= \sum_{\mathbf{k}}(\epsilon^c_{\mathbf{k}}a^\dagger_{c,\mathbf{k}}a_{c\mathbf{k}} - \epsilon^v_{\mathbf{k}}a_{v,\mathbf{k}}a^\dagger_{v\mathbf{k}}) \\ &\approx \sum_{n,m,\mathbf{k},\mathbf{Q}} \frac{\hbar^2k^2}{2\mu}X^\dagger_{n,\mathbf{Q}}X_{m,\mathbf{Q}}\varphi^*_{n,\mathbf{k}}\varphi_{m,\mathbf{k}} + \sum_{n,\mathbf{Q}}\frac{\hbar^2Q^2}{2M}X^\dagger_{n,\mathbf{Q}}X_{n,\mathbf{Q}} \ , \end{aligned}$$

$$H_{e-h} = \sum_{\mathbf{k},\mathbf{k}',\mathbf{q}} V^{cv}_{\mathbf{q}}a^\dagger_{c,\mathbf{k}+\mathbf{q}}a^\dagger_{v,\mathbf{k}'-\mathbf{q}}a_{v,\mathbf{k}'}a_{c,\mathbf{k}} \approx -\sum_{\mathbf{Q},\mathbf{q},\mathbf{k},n} V^{cv}_{\mathbf{q}}X^\dagger_{n,\mathbf{Q}}X_{m,\mathbf{Q}}\varphi^*_{n,\mathbf{k}+\mathbf{q}}\varphi_{m,\mathbf{k}} \ .$$

By making use of the Wannier equation, (2.20), we deduce that $H_0 + H_{e-h} \approx H_{x,0}$ where

$$H_{x,0} = \sum_{n,\mathbf{Q}} E^n_{\mathbf{Q}}X^\dagger_{n,\mathbf{Q}}X_{n,\mathbf{Q}} \ , E^n_{\mathbf{Q}} = E_n + \frac{\hbar^2Q^2}{2M} \ . \tag{2.27}$$

By commuting our new Hamilton operator (2.27) with the excitonic polarization $P_{n,\mathbf{Q}} \equiv \langle X^\dagger_{n,\mathbf{Q}}\rangle$ we directly obtain (2.19) (omitting the band gap E_g). This bosonic Hamiltonian could also have been read off directly from Eq. (2.19). This way of deriving the bosonic Hamiltonian ensures that the equations of motion one obtains in the exciton picture are consistent with the

equations of motion in the electron-hole picture. In the following chapter, we will use this procedure in order to derive an effective interaction Hamiltonian for excitons also taking exciton-exciton interactions into account. Finally, we note that other interaction mechanisms such as exciton-phonon interaction and exciton-photon interactions can also be incorporated into an effective bosonic exciton Hamiltonian in a similar fashion as outlined above [55, 82].

3

Exciton-exciton interactions

A plethora of non-linear quantum phenomena in two-dimensional semiconductors, ranging from anomalous diffusion and non-conventional exciton transport [33, 52, 83] to optical non-linearities [84–86], have been experimentally observed and are attributed to exciton-exciton interactions. Developing a microscopic theory for these many-body interactions has, however, been proven to be challenging due to the underlying fermionic substructure of excitons [35, 87, 88]. In this chapter, we present the many-body Hamiltonian which takes into account exciton-exciton interactions in transition-metal dichalcogenide monolayers and heterobilayers. In particular, we show that intralayer and spatially separated interlayer excitons interact in fundamentally different ways: intralayer exciton-exciton interactions are governed by quantum-mechanical exchange interactions between individual charges and interlayer excitons exhibit predominantly dipolar interactions. Furthermore, we show that the dipolar interactions between layer-hybridized excitons can be efficiently tuned with electric fields.

3.1 Exciton-exciton Hamiltonian

An effective bosonic Hamiltonian which takes into account exciton-exciton interactions can be derived in various ways. As outlined in Ref. [55] and [89] (Paper I), one way of deriving an effective Hamiltonian is to directly trans-

form the purely electronic Coulomb Hamiltonian (2.8) using the pair operator expansions in Eqs. (2.24)-(2.25). It turns out that the resulting Hamiltonian needs to be supplemented by cobosonic correction terms (stemming from the deviation from a bosonic commutator, cf. Eq. (2.23)) and special care has to be taken when evaluating equations of motion with such a Hamiltonian [55]. Here, we therefore instead derive an excitonic Hamiltonian from the equation of motion of the polarization, an approach which was applied on a mean-field level in Ref. [90] (Paper III) and in general in Refs. [91, 92] (Papers IV-V).

The theoretical approach consists of four steps: **i)** find the equation of motion for the polarization $P = \langle a_c^\dagger a_v \rangle$ using the Coulomb Hamiltonian (2.8), **ii)** order the appearing fermionic operators in such a way that they can be replaced by excitonic pair operators and transform the entire equation to the exciton basis, **iii)** make an Ansatz for an excitonic interaction Hamiltonian and commute this Hamiltonian with the excitonic polarization, **iv)** read off the excitonic Coulomb matrix element by demanding that the equations of motion in **ii)** and **iii)** should coincide. The resulting Hamiltonian reads[1]

$$H_{x-x} = \frac{1}{2} \sum_{\substack{\mu,\nu \\ \mathbf{Q},\mathbf{Q}',\mathbf{q}}} G^{\mu\nu\nu\mu}_{\mathbf{Q},\mathbf{Q}',\mathbf{q}} X^\dagger_{\mu,\mathbf{Q}+\mathbf{q}} X^\dagger_{\nu,\mathbf{Q}'-\mathbf{q}} X_{\nu,\mathbf{Q}'} X_{\mu,\mathbf{Q}} \ , \tag{3.1}$$

where $X^{(\dagger)}$ are bosonic creation and annihilation operators, the Greek letters $\mu, \nu = \mathrm{KK}, \mathrm{KK}', \mathrm{K}\Lambda...$ denote excitonic valley indices[2] which could be extended to hold also exciton state or layer degrees of freedom, and $\mathbf{Q}^{(\prime)}$ are exciton center-of-mass momenta. Here, we also restricted ourselves to intravalley and intervalley Coulomb processes involving carriers in the same or different valleys, respectively, but still with a small momentum transfer $\mathbf{q}$. This allows us to study scattering between excitons in different valleys as illustrated in Fig. 3.1. As such the efficiency of the intravalley exciton-exciton scattering process (I, purple) and intervalley exciton-exciton scattering process (II, yellow), as shown in Fig. 3.1, is determined by the excitonic Coulomb matrix elements $G^{\mu\mu\mu\mu}$ and $G^{\mu\nu\nu\mu}$ with $\mu \neq \nu$, respectively. The excitonic

[1] In the Supplemental Material of Ref. [91] we derive a more general Hamiltonian with the interaction matrix element $G^{\alpha\beta\gamma\delta}$, where $\alpha \neq \beta \neq \gamma \neq \delta$. Here, we consider a valley-conserving Hamiltonian.

[2] By convention, the first letter denotes the hole valley and the second letter denotes the electron valley, e.g. a KΛ exciton denotes an exciton composed of a hole in the K-valley and an electron in the Λ-valley. See also Fig. 2.3(a).

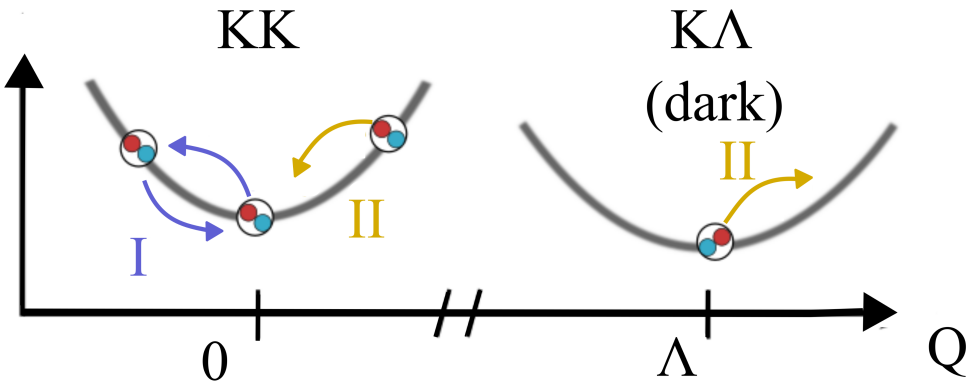

Figure 3.1: Schematic illustration of exciton-exciton scattering channels. We distinguish between intravalley (I, purple) and intervalley (II, yellow) scattering processes. Figure adapted from Ref. [89] (Paper I).

Coulomb matrix element can be expressed as

$$G^{\mu\nu\nu\mu}_{\mathbf{Q},\mathbf{Q}',\mathbf{q}} = V^{\mu\nu\nu\mu}_{\mathrm{dir},\mathbf{q}} + V^{\mu\nu\nu\mu}_{\mathrm{exch},\mathbf{Q},\mathbf{Q}',\mathbf{q}} \,, \tag{3.2}$$

where $V^{\mu\nu\nu\mu}_{\mathrm{dir},\mathbf{q}}$ and $V^{\mu\nu\nu\mu}_{\mathrm{exch},\mathbf{Q},\mathbf{Q}',\mathbf{q}}$ are referred to as direct and exchange exciton-exciton interactions, respectively. The latter incorporates exchange of individual electrons, holes or simultaneous exchange of electrons and holes. As these interactions depend crucially on the screened Coulomb interaction matrix elements V^{cc}, V^{vv} (intraband elements) and $V^{cv}, \bar{V}^{cv}$ (interband elements, cf. Fig. 2.2) their explicit form differ depending on whether interactions between intralayer excitons in a monolayer or interlayer excitons in a bilayer are considered. Both cases are therefore discussed separately below.

3.2 Monolayer excitons

Direct interaction

In the case of TMD monolayers, it holds that the dominant long-range part of the Coulomb interaction $V^{\lambda\lambda'}_{\mathbf{q}} \approx V_{\mathbf{q}}$ and is dependent on the dielectric function $\varepsilon_{\mathbf{q}}$ which takes into account screening from the surrounding sub-

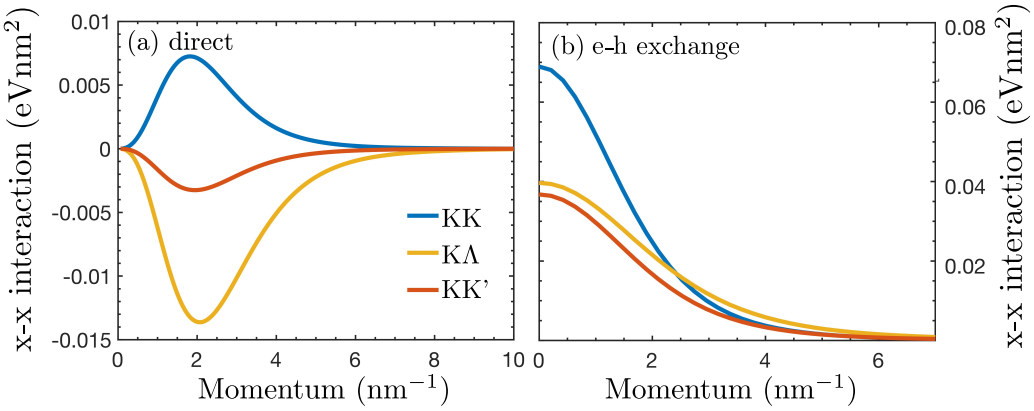

Figure 3.2: Intravalley (KK, blue) and intervalley (KK', red, KΛ, yellow) exciton-exciton interactions in a WSe_2 monolayer. Figure adapted from Ref. [89] (Paper I).

strate and TMD layer itself, cf. Eq. (2.10).[3] Hence, we find that the direct part of the exciton-exciton interaction reads

$$V^{\mu\nu\nu\mu}_{\mathrm{dir},\mathbf{q}} = \frac{1}{2} V_{\mathbf{q}} \Big(F_{\mu\mu}(\beta^{\mu}\mathbf{q}) - F_{\mu\mu}(-\alpha^{\mu}\mathbf{q}) \Big) \Big(F_{\nu\nu}(\beta^{\nu}\mathbf{q}) - F_{\nu\nu}(-\alpha^{\nu}\mathbf{q}) \Big)^{*} \ , \quad (3.3)$$

where we defined the form-factors $F_{\mu\mu}(x\mathbf{q}) = \sum_{\mathbf{k}} \varphi^{*}_{\mu,\mathbf{k}} \varphi_{\mu,\mathbf{k}+x\mathbf{q}}$, dependent on the excitonic wave functions as obtained from the Wannier equation (Eq. (2.20)) and the electron and hole masses through $\beta = m_h/(m_e + m_h)$ and $\alpha = m_e/(m_e + m_h)$. Intriguingly, we note that this part of the interaction gets boosted by increasing the mass asymmetry of the electronic constituents involved in the scattering processes, as shown in Fig. 3.2(a). In particular, considering scattering between KK and KΛ excitons (process II in Fig. 3.1), we obtain a more efficient scattering due to the large mass asymmetry between holes at the K-point and electrons at the Λ-point. By expanding Eq. (3.3) for small momentum and expressing the form-factors in real space via the Fourier transform we can gain additional insights in the direct matrix element,

$$V^{\mu\nu\nu\mu}_{\mathrm{dir},\mathbf{q}} \sim V_{\mathbf{q}} r^2_{\mu,\mathrm{B}} r^2_{\mu,\mathrm{B}} q^4 Q_{\mu} Q_{\nu} \text{ (for small } q) \ . \quad (3.4)$$

[3]The Coulomb interaction is also principally screened by other charge complexes in the material at elevated densities. This issue is addressed in Section 4.1.

Here, we introduced the effective exciton charge

$$Q_\mu = \frac{m^{\mu_e} - m^{\mu_h}}{m^{\mu_e} + m^{\mu_h}} \ , \tag{3.5}$$

and the exciton Bohr radius $r_{\mu,\mathrm{B}} = \sqrt{\langle\mu|r^2|\mu\rangle}$. Importantly, we note that the direct interaction for monolayers is vanishing for $q = 0$ and that the nature of the interaction is either repulsive or attractive depending on the sign of the excitonic charge. Note that Q_μ should not be thought of as an electromagnetic charge, but rather as a polarizability where the large mass imbalance in electron and hole constituents polarizes the excitons to effectively become less neutral, making them interact stronger.

Exchange interactions

Moving on to the exchange part of the Hamiltonian, there are two contributions to consider, one contribution being responsible for carrier-carrier exchange ($\sim V$) and one contribution due to electron-hole exchange interactions ($\sim \bar{V}$), cf. Fig. 2.2. In particular, we find for the latter contribution (setting $\mathbf{Q} = \mathbf{Q}' = 0$ for simplicity)

$$V^{\mu\nu\nu\mu}_{\mathrm{exch},0,0,\mathbf{q}}|_{\mathrm{e-h\ exch.}} = (\delta_{\mu_h,\nu_e} U^{\mu\nu}_{\mathbf{q}} + \delta_{\nu_h,\mu_e} U^{\nu\mu}_{-\mathbf{q}}) \ , \tag{3.6}$$

with $U^{\mu\nu}_{\mathbf{q}} = \sum_{\mathbf{q}_1,\mathbf{q}_2} \bar{V}^{\mu\nu}_{\mathbf{q}_2-\mathbf{q}_1} R_\mu(\mathbf{q}_1, \alpha^\mu \mathbf{q}) R_\nu(\mathbf{q}_2, \beta^\nu \mathbf{q})$ introducing the function $R_\mu(\mathbf{q}_1, x\mathbf{q}) = \varphi^*_{\mu,\mathbf{q}_1} \varphi_{\mu,\mathbf{q}_1+x\mathbf{q}}$ and the electronic electron-hole exchange interaction $\bar{V}^{\mu\nu}_{\mathbf{q}} = V_{\mathbf{q}} (\mathbf{q} \cdot \mathbf{M}_{\mu_h})(\mathbf{q} \cdot \mathbf{M}_{\nu_e})^*$ with M being the optical matrix element. As shown in Fig. 3.2(b), the exchange interaction strength dominates over the direct interaction strength in TMD monolayers by almost an order of magnitude. Furthermore, it is always repulsive and non-vanishing at $q = 0$. Moreover, it is not as sensitive in changes in electron and hole masses as the direct interaction. Finally, the carrier-carrier exchange contribution reads [35, 90, 93]

$$V^{\mu\nu\nu\mu}_{\mathrm{exch},0,0,\mathbf{q}}|_{\mathrm{c-c\ exch.}} = \delta_{\mu_e,\nu_e} X^{\mu\nu}(\mathbf{q}, \alpha^\mu, \beta^\nu) + \delta_{\mu_h,\nu_h} X^{\mu\nu}(-\mathbf{q}, \beta^\mu, \alpha^\nu) \ , \tag{3.7}$$

where $X^{\mu\nu}(\mathbf{q}, \alpha^\mu, \beta^\nu) = \frac{1}{2} \sum_{\mathbf{k},\mathbf{k}'} V_{\mathbf{k}-\mathbf{k}'} (\varphi_{\mu,\mathbf{k}'-\mathbf{q}} - \varphi_{\mu,\mathbf{k}-\mathbf{q}}) \varphi^*_{\mu,\mathbf{k}-\alpha^\mu\mathbf{q}} \varphi^*_{\nu,\mathbf{k}'-\beta^\nu\mathbf{q}} \varphi_{\nu,\mathbf{k}'}$ and the Kronecker deltas ensure that exchange of individual carriers (electrons or holes) can only take place if the electrons or holes reside at the same

high-symmetry point. The momentum-dependence of the carrier-carrier exchange interaction is qualitatively the same as the electron-hole exchange interaction as has been reported in Ref. [35,94] for single layer TMDs and quantum wells, respectively. Note that both exchange contributions in Eq.(3.6)-(3.7) are generally repulsive and result in a net repulsive exciton-exciton interaction in TMD monolayers.[4] In Paper III and in Section 4.1, we show that this contribution to the exciton-exciton interaction results in significant density-dependent energy renormalizations for excitons in a single TMD monolayer.

3.3 Interlayer excitons in heterobilayers

When vertically stacking two or more transition-metal dichalcogenide monolayers together a van der Waals heterostructure is obtained, which enables the formation of long-lived interlayer excitons, i.e., excitons composed of electrons and holes in different layers [95]. Due to the increased dielectric screening from the other layer and weak Coulomb interaction between spatially separated charges, interlayer exciton binding energies are significantly smaller than the exciton binding energies in a monolayer. In particular, considering KK interlayer excitons in hBN-encapsulated $MoSe_2$-WSe_2 heterostructures we deduce a binding energy of around 90 meV [89], which is approximately half of the binding energy of the bright exciton in monolayer WSe_2, cf. Fig. 2.4(b). Still, the type-II band alignment (Fig. 1.2(b)) in $MoSe_2$-WSe_2 makes the formation of interlayer excitons highly favorable and, in fact, interlayer exciton states are rendered the energetically lowest states in these structures as has been verified by microscopic calculations [96, 97], time-resolved photoluminescence measurements [50, 85, 98] and tr-ARPES measurements [44].

In order to generalize the exciton-exciton interaction in Eq. (3.1) to interlayer excitons, we have to take into account the fact that the Coulomb

[4]The carrier-carrier exchange, Eq. (3.7), is not present in the bosonic Hamiltonian discussed in Paper I. However, importantly, the conclusion that exciton-exciton interactions between intralayer excitons are predominantly due to exchange effects still holds. Moreover, as shown in Ref. [55], the Hamiltonian considered in Paper I can still be employed to study exciton dynamics.

interaction between spatially separated electrons and holes is weaker than the Coulomb interaction between charges within a single TMD layer. By introducing layer indices l and $\bar{l}$ for the two layers and modifying the Coulomb matrix elements $V_{\mathbf{q}}^{cc} \to V_{\mathbf{q}}^{c_l c_l} = V_{\text{bare},\mathbf{q}}/\varepsilon_{\mathbf{q}}^{ll}$, $V_{\mathbf{q}}^{vv} \to V_{\mathbf{q}}^{v_{\bar{l}} v_{\bar{l}}} = V_{\text{bare},\mathbf{q}}/\varepsilon_{\mathbf{q}}^{\bar{l}\bar{l}}$ and $V_{\mathbf{q}}^{cv} \to V_{\mathbf{q}}^{c_l v_{\bar{l}}} = V_{\text{bare},\mathbf{q}}/\varepsilon_{\mathbf{q}}^{l\bar{l}}$ with layer-dependent dielectric functions [51, 99], the direct exciton-exciton interaction, which previously just included interactions between intralayer excitons (abbreviated X-X), is generalized to interlayer exciton-exciton interactions (IX-IX) and intralayer-interlayer interactions (IX-X) . Here, we will not provide the full expressions for these interactions, but in analogy to (3.4), consider the small q limit for the interlayer exciton-exciton interaction. In this case, one finds

$$V_{\text{dir},\mathbf{q}}^{\text{IX}-\text{IX}} \sim \frac{e_0^2}{2\epsilon_0}\left[\frac{d_1}{\varepsilon_{\perp}^{(1)}} + \frac{d_2}{\varepsilon_{\perp}^{(2)}})\right] + \mathcal{O}(\mathbf{q}) \text{ (for small } q) \,, \tag{3.8}$$

where d_i are the TMD layer thicknesses and $\varepsilon_{\perp}^{(i)}$ are perpendicular components of the dielectric tensor of the TMDs, the latter being extracted from

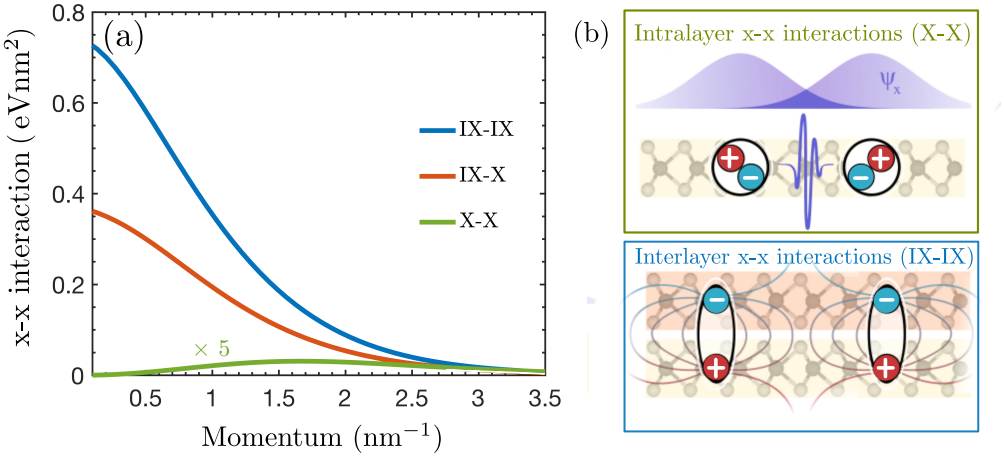

Figure 3.3: Interlayer (IX) and intralayer (X) exciton-exciton interactions in $MoSe_2$-WSe_2 heterostructures. (a): Momentum space representation of interaction matrix elements. Interlayer excitons exhibit a permanent out-of-plane dipole moment and hence interact much stronger than intralayer excitons. (b): Schematic illustration of intralayer and interlayer exciton-exciton interactions. Figures adapted from Ref. [89] (Paper I).

DFT calculations [100]. By inspection, the direct interlayer exciton-exciton interaction is a dipole-dipole interaction, where the layer thicknesses d_i determine the separation between electrons and holes and thereby the out-of-plane dipole moment of the interlayer excitons. Similarly, one finds that the interaction between intralayer excitons in a heterostructure, $V_{\mathrm{dir},\mathbf{q}}^{\mathrm{X-X}}$, scales with $V_q q^4$ as in the monolayer case, and that the mixed interaction between intra- and interlayer excitons, $V_{\mathrm{dir},\mathbf{q}}^{\mathrm{X-IX}}$ attains a constant value in the limit $q \to 0$, reflecting the permanent out-of-plane dipole moment of the IX.

The full momentum-dependent matrix elements are shown in Fig. 3.3(a), revealing a strong repulsive interaction for all q for interlayer interactions, reflecting the dipolar nature of spatially separated electron-hole pairs. We have also, in the Supplementary Material of Paper IV, explicitly shown that the direct interlayer exciton-exciton interaction in real space can be well approximated as a dipolar interaction at large distances, i.e. $V_{\mathrm{dir}}^{\mathrm{IX-IX}}(\mathbf{r}) = \sum_{\mathbf{q}} \mathrm{e}^{i\mathbf{q}\cdot\mathbf{r}} V_{\mathrm{dir},\mathbf{q}}^{\mathrm{IX-IX}} \sim \frac{d^2}{\epsilon|\mathbf{r}|^3} + \mathcal{O}(|\mathbf{r}|^{-5})$. The mechanisms governing the exciton-exciton interactions between intra- and interlayer excitons are hence fundamentally different: the intralayer interaction is governed by excitonic wave function overlaps and the (direct) interaction between interlayer excitons is a result of strong dipole-dipole repulsion (Fig. 3.3(b)).

The exchange contributions to the interlayer exciton-exciton interaction can be obtained in a similar fashion as the direct dipole-dipole repulsion. As shown in Paper III, however, these contributions are significantly smaller than the direct contributions. In particular, we find that the carrier-carrier exchange is highly dependent on the layer separation and is generally weak and attractive when the layer separation becomes comparable to the exciton Bohr radius [90]. Furthermore, due to the spatial separation of electrons and holes forming the interlayer exciton in a heterostructure, their optical matrix element is suppressed, and consequently the corresponding electron-hole exchange contributions are completely negligible. The tunability of interlayer exciton-exciton interactions with layer separation is further discussed in the context of interlayer exciton transport in Section 5.2.

3.4 Layer-hybridized excitons in homobilayers

In a general transition-metal dichalcogenide bilayer, electrons and holes do not have to be confined to individual layers, but can display significant interlayer tunneling. As a result, layer-hybridized excitons are formed, where the constituent electrons or holes are delocalized across the two layers (cf. Fig. 3.4) [80]. The formation of such excitons is particularly favored in homobilayers, in contrast to in the type-II $MoSe_2$-WSe_2 heterostructure considered previously, where the dominating exciton species have interlayer character. As layer-hybridized excitons have a non-zero interlayer component, they also carry an out-of-plane dipole moment which can couple efficiently to out-of-plane electric fields. In Paper IV, we investigate the large electrical tunability of the dipole-dipole repulsion between hybrid excitons in naturally stacked[5] WSe_2 homobilayers. In particular, taking WSe_2 homobilayers as an example, we find that these structures exhibit a rich hybrid exciton landscape involving momentum-dark hybridized excitons with varying layer composition (Fig. 3.4(a)). In the following, we show how the theoretical framework introduced in Chapter 2 and above is used to treat hybrid exciton-exciton interactions.

We microscopically access the hybrid exciton landscape by diagonalizing the Hamiltonian

$$H_{x,0} = \sum_{\xi,L,L',\mathbf{Q}} (E^{\xi}_{L,\mathbf{Q}}\delta_{L,L'} + T^{\xi}_{LL'}) X^{\dagger\xi}_{L,\mathbf{Q}} X^{\xi}_{L',\mathbf{Q}} \, . \tag{3.9}$$

Here, $E^{\xi}_{L,\mathbf{Q}}$ is the layer (L) and valley (ξ)-dependent center-of-mass dispersion, i.e. a generalization of Eq. (2.27) to multiple layers and valleys. The layer index $L = (l_h, l_e)$ and valley index $\xi = (\xi_h, \xi_e)$ are compound indices taking into account both electron and hole degrees of freedom. Furthermore, $T^{\xi}_{LL'}$ is the valley-specific excitonic tunneling matrix element which describes the tunneling of individual electrons/holes between the two layers. The tunneling matrix elements are dependent on excitonic wave function overlaps

[5]This stacking configuration is also referred to as 2H-stacking or anti-parallel stacking, where the constituent monolayers are rotated 180° with respect to each other. Other stacking configurations, such as R-type stacking are also possible [80, 97].

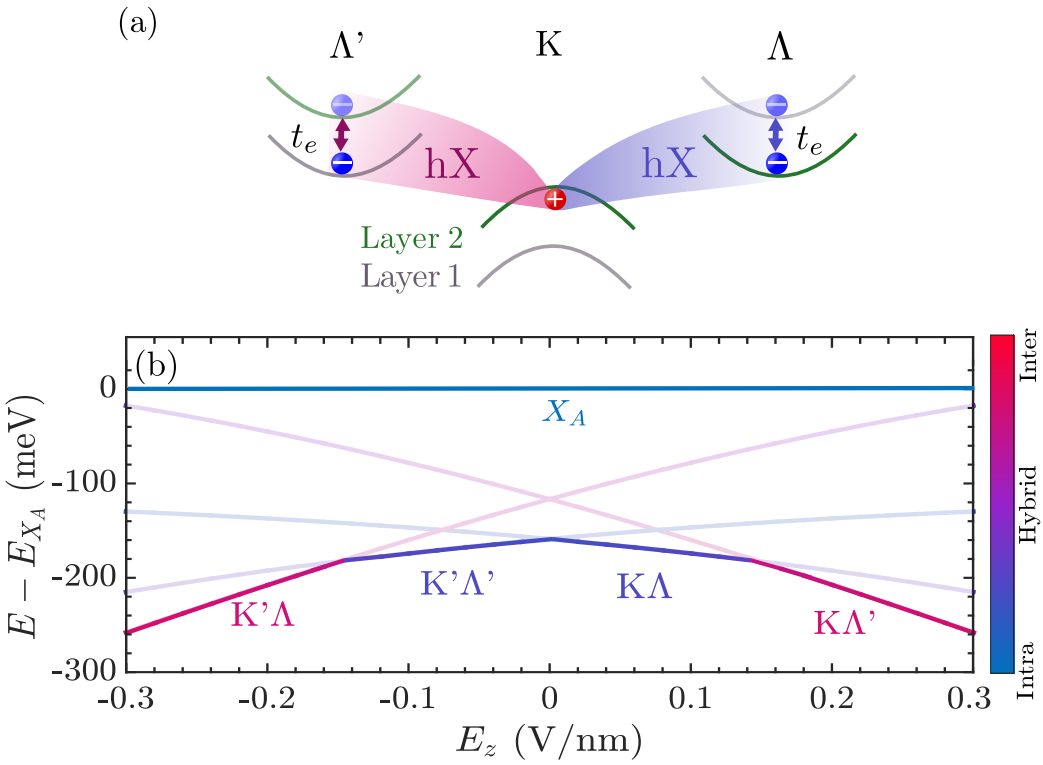

Figure 3.4: Electrical field tuning of hybrid excitons in naturally stacked WSe_2 homobilayers. (a): Mostly intralayer-like KΛ (interlayer-like KΛ′) hybrid excitons are predominantly formed via electron tunneling at the Λ-point (Λ'-point). (b): Exciton landscape in WSe_2 homobilayers as function of electric field. A transition from a mostly intralayer-like KΛ/K'Λ' exciton ground state to an mostly interlayer-like KΛ'/K'Λ exciton ground state occurs at $|E_z| > 0.15$ V/nm. Figure adapted from Ref. [91] (Paper IV).

and electron/hole tunneling strengths, where the latter are obtained from *ab-initio* calculations and reported for all common TMD bilayers in Ref. [97]. In the considered naturally stacked WSe_2 homobilayer, the Hamiltonian above can be expressed as 4 by 4 matrix coupling the intralayer ($L = \mathrm{X}_1, \mathrm{X}_2$) and interlayer ($L = \mathrm{IX}_1, \mathrm{IX}_2$) excitons via interlayer tunneling. We also include an out-of-plane electric field in our calculations by exploiting the quantum-confined Stark effect such that the interlayer exciton energy becomes renormalized as $E^{\xi}_{\mathrm{IX},\mathbf{Q}} \to E^{\xi}_{\mathrm{IX},\mathbf{Q}} + d_{\mathrm{TMD}} e_0 E_z$, with the dipole length d_{TMD} taken as the TMD thickness and E_z being the electric field. In order to diagonalize

the Hamiltonian in (3.9), we perform a transformation to a hybrid exciton basis such that $X^{\dagger\xi}_{L,\mathbf{Q}} = \sum_\eta C^{\xi\eta}_L(\mathbf{Q}) Y^{\dagger\xi}_{\eta,\mathbf{Q}}$, introducing hybrid exciton operators $Y^{(\dagger)}$. By solving the resulting eigenvalue problem for the mixing coefficients $C^{\xi\eta}_L(\mathbf{Q})$, we gain access to both hybrid exciton energies and the probability $|C^{\xi\eta}_L(\mathbf{Q})|^2$ which determines the amount of intra- and interlayer components of hybrid excitons.

In Fig. 3.4(b), the electric-field dependent exciton landscape in WSe_2 homobilayers is shown. We find that the exciton ground state at vanishing electric fields is a momentum-dark KΛ exciton state appearing ~ 160 meV below the bright A exciton, in agreement with previous Bethe-Salpeter calculations [101] and luminescence experiments [102, 103]. Importantly, as natural (H-type) stacking is considered here where the two monolayers forming the bilayer are rotated 180 degrees with respect to each other such that e.g. the K-point of one the layers reside on the K'-point of the other layer in momentum space. As a consequence, the ordering of spin-split bands is effectively inverted in one of the layers [80]. This results in a two-fold degenerate ground state with a K'Λ' state which carries an opposite dipole moment to the KΛ state. Moreover, the ground state is strongly hybridized and intralayer-like ($|C^{\mathrm{K\Lambda}}_{\mathrm{X}}|^2 \approx 0.77$, cf. colorbar), where the hybridization is induced predominantly via electron tunneling at the Λ-point [80, 97, 101]. Furthermore, in close vicinity of the KΛ/K'Λ' states lies a mostly interlayer-like KΛ'-state (cf. the band ordering in Fig. 3.4(a)).

Considering the effect of applying an out-of-plane electric field on the exciton landscape, focusing on the case $E_z > 0$, we predict a transition in the exciton ground state from the mostly intralayer-like two-fold degenerate ground state to the KΛ' state at $E_z \approx 0.15$ V/nm. This is due to the strong coupling to electric fields of KΛ' excitons owing to their large interlayer component ($|C^{\mathrm{K\Lambda'}}_{\mathrm{IX}}|^2 \approx 0.64$ at vanishing fields). Signatures of the transition in exciton ground state with electric fields have also been observed by means of electric-field dependent photoluminescence measurements at low temperature, cf. Ref. [92, 102, 104] and Paper V. The remarkable interplay between different hybrid exciton ground states as a function of electric field becomes even more intriguing at elevated densities, where exciton-exciton interactions become important. In particular, focusing on the dipolar part of the exciton-exciton interaction, we may distinguish between two fundamentally different interaction regimes at low and high electric fields involving weakly interact-

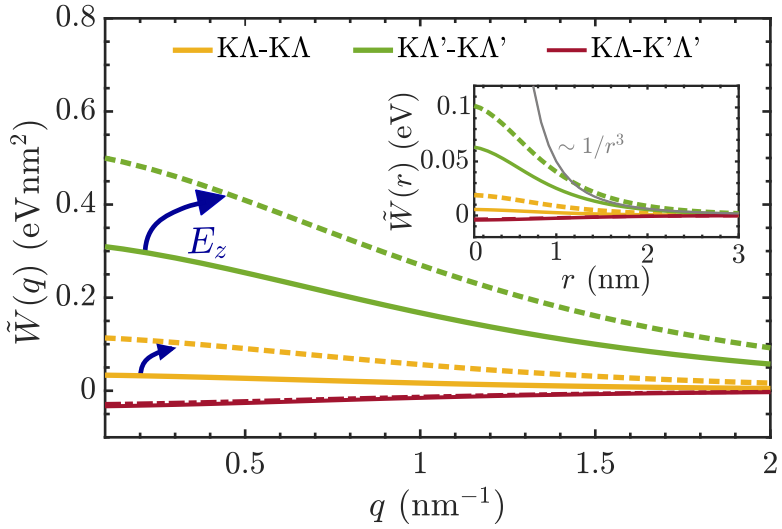

Figure 3.5: Electrical field tuning of hybrid exciton-exciton interactions in naturally stacked WSe_2 homobilayers. The interactions at vanishing electric fields ($E_z = 0$) and at finite fields ($E_z = 0.3$ V/nm) are shown as solid and dashed lines, respectively. Figure adapted from Ref. [91] (Paper IV).

ing KΛ/K'Λ' excitons and strongly dipolar KΛ'/K'Λ excitons, respectively. These regimes can be described by generalizing the exciton-exciton interaction (3.1) to layer-hybridized excitons and transform the Hamiltonian to a hybrid basis

$$\tilde{H}_{x-x} = \frac{1}{2} \sum_{\xi,\xi',\mathbf{Q},\mathbf{Q}',\mathbf{q}} \tilde{W}_{\mathbf{q}}^{\xi\xi'} Y_{\xi,\mathbf{Q}+\mathbf{q}}^{\dagger} Y_{\xi',\mathbf{Q}'-\mathbf{q}}^{\dagger} Y_{\xi',\mathbf{Q}'} Y_{\xi,\mathbf{Q}} \ , \tag{3.10}$$

with $\tilde{W}_{\mathbf{q}}^{\xi\xi'} = \sum_{L,L'} V_{L,L',\mathbf{q}}^{\xi\xi'} |C_L^{\xi}|^2 |C_{L'}^{\xi'}|^2$, C_L^{ξ} being mixing coefficients determining the intra- ($L = \mathrm{X}$) and interlayer ($L = \mathrm{IX}$) composition of the hybrid exciton in valley ξ. Here, we also assumed that the mixing coefficients depend only weakly on momentum, which holds well in an untwisted homobilayer where the momentum transfer via tunneling is small, and consider only the lowest hybrid exciton state η. Importantly, the hybrid exciton-exciton interaction mixes contributions from both intra- and interlayer exciton species and weights the interaction with the corresponding mixing coefficients.

In Fig. 3.5, the electric-field dependent hybrid exciton-exciton interaction strength is shown for different valley species in a WSe_2 homobilayer. We find

both repulsive interactions between excitons with the same valley configuration (green and yellow lines) and weakly attractive interactions between KΛ and K'Λ' excitons, reflecting their opposite dipole moments. Furthermore, as expected, the interaction is most repulsive between KΛ' excitons which carry the largest out-of-plane dipole moment. We also confirm, by considering the interaction in real space, that the hybrid exciton-exciton interaction between mostly interlayer-like excitons (green lines) resembles a dipole-dipole interaction ($\sim 1/r^3$) in the long wavelength limit (cf. inset). Finally, we note that both the KΛ-KΛ and the KΛ'-KΛ' exciton-exciton interactions are enhanced with electric fields. This enhancement is explained by the increase in interlayer component at elevated fields. In contrast, as KΛ and K'Λ' excitons carry opposite dipole moments, the mixing coefficient for one of the excitons is increased meanwhile the mixing coefficient for the other exciton is decreased resulting in the weak electric field dependence of the KΛ-K'Λ' exciton-exciton interaction (red lines).

Having discussed the fundamental interaction mechanisms between intralayer, interlayer and layer-hybridized excitons, we have set the stage for investigating how these mechanisms become manifest in high-excitation experiments. In the following chapters, Chapters 4-5, we show how the exciton-exciton Hamiltonian can be used to study density-dependent shifts of exciton resonances and non-linearities in exciton transport.

4

Coulomb-induced many-body effects in optical spectra

In the previous chapter we provided the theoretical foundation for the exciton-exciton interaction in mono- and bilayer transition-metal dichalcogenides. Here, we show that the exciton Hamiltonian can be used to compute density-dependent exciton energy renormalizations which become manifest in experiments and optical spectra as excitation power-dependent shifts of exciton resonances (Paper III). In particular, we emphasize the crucial role of dipole-dipole repulsion between interlayer excitons, but also shed light on different interaction mechanisms such as carrier-carrier exchange and higher-order correlation effects. Moreover, electric fields are shown to provide important tuning knobs for the control of non-linearities in optical spectra in homobilayers (Papers IV-V).

4.1 Density-dependent exciton line shifts

In order to study how exciton resonances shift with exciton density, the equation of motion for the excitonic polarization $P_{\zeta,\mathbf{Q}} = \langle X^\dagger_{\zeta,\mathbf{Q}} \rangle$ is considered, where ζ is a general compound index which could include e.g. valley, layer or the exciton state index. Considering Heisenberg's equation of motion with the Hamiltonian $H = H_{x,0} + H_{x-x}$ with $H_{x,0}$ defined in Eq. (2.27) and H_{x-x}

in Eq. (3.1) (with general quantum numbers) on a Hartree-Fock level we find

$$\frac{d}{dt}P_{\zeta,\mathbf{Q}} = \frac{i}{\hbar}E_{\zeta,\mathbf{Q}}P_{\zeta,\mathbf{Q}} + \frac{i}{\hbar}\sum_{\zeta',\mathbf{q}}(G^{\zeta\zeta'\zeta'\zeta}_{\mathbf{Q},\mathbf{q},0} + G^{\zeta'\zeta\zeta'\zeta}_{\mathbf{Q},\mathbf{q},\mathbf{q}-\mathbf{Q}})N^{\zeta'}_{\mathbf{q}}P_{\zeta,\mathbf{Q}} \ , \tag{4.1}$$

where we here assumed a spatially homogenous system, i.e. set $\langle X^\dagger_{\zeta,\mathbf{Q}}X_{\zeta',\mathbf{Q}'}\rangle = \delta^{\zeta,\zeta'}_{\mathbf{Q},\mathbf{Q}'}N^\zeta_{\mathbf{Q}}$, N being the exciton occupation and made use of the random phase approximation [105] to factorize the equation in terms of occupations and polarizations.[1] An important special case, which was considered in Paper III, is obtained by assuming that the dynamics is governed by a single exciton species, $\zeta \equiv \zeta_0$, which is a good approximation at low temperatures. Furthermore, at low temperatures, the exciton distribution is strongly peaked around vanishing momenta, such that $N_{\mathbf{q}} \sim n_x\delta_{\mathbf{q},0}$, n_x being the total exciton density. Within these approximations and defining $P_{\zeta_0,\mathbf{Q}=0} \equiv P_{\zeta_0}$ and $2G^{\zeta_0\zeta_0\zeta_0\zeta_0}_{0,0,0} \equiv G_0$

$$\frac{d}{dt}P_{\zeta_0} = \frac{i}{\hbar}(E_{\zeta_0} + \Delta E_{\mathrm{HF}}(n_x))P_{\zeta_0} \ , \Delta E_{\mathrm{HF}}(n_x) = G_0 n_x \ . \tag{4.2}$$

We note that the quantity $\Delta E_{\mathrm{HF}}(n_x)$ renormalizes the bare exciton energy E_{ζ_0} as function of density. Importantly, the equation above is the excitonic analogue of Eq. (2.14), where the carrier occupations (f^c, f^v) entering Eq. (2.14) have here been transferred to excitonic occupations (N).

In Paper III, we also consider contributions beyond Hartree-Fock theory by including correlation effects in the form of excitonic screening [106]. At elevated densities, below the Mott transition and assuming that all electron-hole pairs are bound, excitons screen each other [106], analogous to how electrons or holes screen each other in a semiconductor [107]. This induces a density-dependence also in the interaction matrix elements as well as in the electronic

[1] Here, we note that, before factorization, the polarization couples to a three-operator expectation value $\propto \langle X^\dagger_1 X^\dagger_2 X_3\rangle$. Since we derived the exciton-exciton Hamiltonian from the corresponding equation of motion for the microscopic polarization in the electron-hole picture we explicitly include terms associated with carrier-carrier exchange at the level of the Hamiltonian and can straightforwardly expand appearing three-operators quantities as bosonic operators. In Ref. [55], it is shown that a Hamiltonian without carrier-carrier exchange can also be used, but then the factorization of bosonic operators is more involved. Still, independently of which Hamiltonian is used, the resulting equations of motion coincide.

band gap and modifies the energy renormalization $\Delta E_{\mathrm{HF}}(n_x) \rightarrow \Delta E(n_x)$ with

$$\Delta E(n_x) = \tilde{G}_0 n_x + \Sigma_{CH} \ , \tag{4.3}$$

where $\tilde{G}_0$ is the screened excitonic matrix elements being dependent on the screened electronic Coulomb interaction $\tilde{V}_{\mathbf{q}} = V_{\mathbf{q}}/\varepsilon_{\mathrm{exc}}(\mathbf{q})$, $\varepsilon_{\mathrm{exc}}(\mathbf{q})$ being the static dielectric screening due to Coulomb-bound electron-hole pairs. The second term in Eq. (4.3) is the Coulomb hole, $\Sigma_{CH} = \sum_{\mathbf{q}}(V^{vv}_{\mathbf{q}}/\varepsilon_{\mathrm{exc}}(\mathbf{q}) - V^{vv}_{\mathbf{q}})$ which describes the reduction of single-particle energies at high densities [108] and in our formalism enters as a renormalization due to the fully occupied valence band. We consider the long wavelength limit ($q \rightarrow 0$) of the exciton-exciton interaction for intra- and interlayer excitons, here denoted $\tilde{G}_0^{\mathrm{X-X}}$ and $\tilde{G}_0^{\mathrm{IX-IX}}$, respectively. These momentum-independent matrix elements can be separated into direct and exchange contributions as $\tilde{G}_0^{L-L} = g^L_{d-d} + g^L_{x-x}$, $L = $ X,IX and are obtained from Eq. (3.2), (3.6), (3.7) and (3.8). The direct contributions read

$$g^{\mathrm{X}}_{d-d} = 0 \ , g^{\mathrm{IX}}_{d-d} = \frac{e_0^2}{2\epsilon_0}\left[\frac{d_1}{\varepsilon^{(1)}_{\perp}} + \frac{d_2}{\varepsilon^{(1)}_{\perp}}\right] \tag{4.4}$$

and dominant intra- and interlayer exchange contributions due to carrier-carrier exchange are given by[2]

$$\begin{aligned} g^{\mathrm{X}}_{x-x} &= 2\sum_{\mathbf{k},\mathbf{k}'} \tilde{V}_{\mathbf{k}-\mathbf{k}'}(\varphi_{\mathrm{X},\mathbf{k}'} - \varphi_{\mathrm{X},\mathbf{k}})\varphi^*_{\mathrm{X},\mathbf{k}}\varphi^*_{\mathrm{X},\mathbf{k}'}\varphi_{\mathrm{X},\mathbf{k}'} \\ g^{\mathrm{IX-IX}}_{x-x} &= \sum_{\mathbf{k},\mathbf{k}'}(2\tilde{V}^{c_l v_{\bar{l}}}_{\mathbf{k}-\mathbf{k}'}\varphi_{\mathrm{IX},\mathbf{k}'} - (\tilde{V}^{c_l c_l}_{\mathbf{k}-\mathbf{k}'} + \tilde{V}^{v_{\bar{l}} v_{\bar{l}}}_{\mathbf{k}-\mathbf{k}'})\varphi_{\mathrm{IX},\mathbf{k}})\varphi^*_{\mathrm{IX},\mathbf{k}}\varphi^*_{\mathrm{IX},\mathbf{k}'}\varphi_{\mathrm{IX},\mathbf{k}'} \ . \end{aligned} \tag{4.5}$$

Here, $\varphi_{L,\mathbf{k}}$ with $L = \mathrm{X}, \mathrm{IX}$ are intralayer and interlayer exciton wave functions and $\tilde{V}^{\lambda_l\lambda_l}, \tilde{V}^{\lambda\bar{\lambda}_{\bar{l}}}$, $\lambda = c,v$ are screened intra- and interlayer Coulomb interactions, respectively.

In Fig. 4.1, we show the density dependence of the energy renormalization, ΔE, (Eq. (4.3)) for intralayer excitons (X) in a WSe_2 monolayer and interlayer excitons (IX) in a $MoSe_2$-WSe_2 heterobilayer. Importantly, we obtain a net blue-shift of 15 meV for interlayer excitons at the exciton density

[2]One also obtains a minor repulsive correction to the intralayer energy renormalization due to electron-hole exchange, but here we focus on the dominant terms and refer the interested reader to the Supplementary Material of Paper III for a more general derivation.

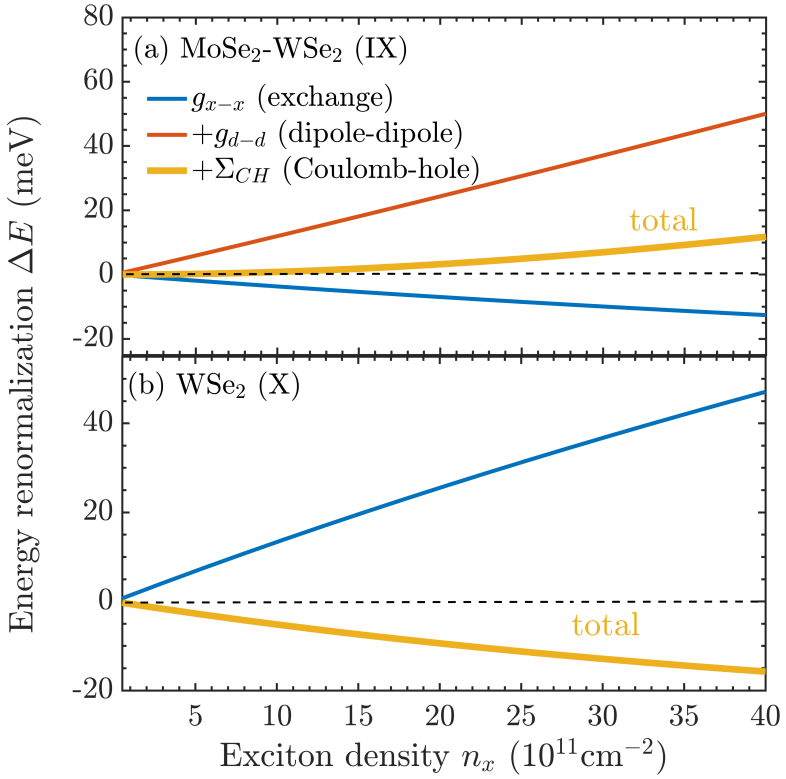

Figure 4.1: Density-dependent exciton line shifts in hBN-encapsulated $MoSe_2$-WSe_2 heterobilayers and WSe_2 monolayers respectively. Individual contributions are added up consecutively. (a) Interlayer exciton line shifts as a function of exciton density, n_x including dipole-dipole, exchange interactions and Coulomb-hole contributions. (b) Intralayer exciton line shifts. Figure taken from Ref. [90] (Paper III).

$n_x = 4 \cdot 10^{12}$ cm^{-2} as a result of strong dipole-dipole interactions- in qualitative agreement with experimental studies [85] and a similar red-shift for intralayer excitons when increasing pump power, which we explain through the interplay of Coulomb-induced repulsive and attractive interactions. The contributions due to exchange differ qualitatively comparing intra- and interlayer excitons, with the exchange contribution being strongly repulsive in the intralayer case and weakly attractive in the intralayer case. As can be seen in Eq. (4.5), the exchange contribution to the energy renormalization is dependent on both electron-hole interaction and the carrier-carrier

interaction. The electron-hole interaction is much weaker than the carrier-carrier interaction for interlayer excitons as electrons and holes are confined to different layers and exhibit significant screening. In general, these interactions are sensitive to changes in layer separation, and the strength of the exchange interaction is significantly reduced as the electron-hole separation becomes of the order of the exciton Bohr radius and excitonic wave function overlaps become small [109, 110]. Furthermore, the Coulomb-hole term, which includes the mutual Coulomb repulsion between holes in the valence band, results in a significant reduction of the line shifts for both intra- and interlayer resonances.

The predicted line-shifts for interlayer excitons are in good agreement with previous experiments [52, 85, 111]. Comparing previous power-dependent line-shifts in experiments [33, 85, 86] and theory, we note that the obtained energy renormalizations for intralayer excitons are overestimated. Photoluminescence experiments reveal that the shift of exciton resonances in TMD monolayers with density is suppressed and of the order of 1 meV at densities, $n_x \sim 10^{12}$ cm^{-2} [33]. A better agreement between theory and experiment could potentially be achieved by treating screening in a more sophisticated way, e.g. using a model which incorporates dynamic screening effects [30,112] . Furthermore, it has recently been suggested that interactions between excitons and higher-order charge complexes such as biexcitons could reduce the shifts of exciton resonances in TMD monolayers considerably [86]. Guided by many-body calculations and state-of-the-art experiments, we will therefore disregard the intralayer exchange renormalizations and focus on the dipolar interlayer part of the exciton-exciton interaction when discussing density-dependent luminescence shifts of layer-hybridized excitons in the following.

4.2 Electrically tunable dipole lengths of hybrid excitons

The Heisenberg equation of motion for the polarization as presented in Eq. (4.2) can also be generalized to hybrid excitons, starting from the hybrid exciton Hamiltonian (3.10) and excitonic polarization expressed in a hybrid exciton basis as discussed in Paper IV. As the calculation of the corresponding

energy renormalization ΔE is analogous to the calculation done above, we will just provide the final expression for the hybrid energy renormalization on a Hartree-Fock level (see Paper IV for details)

$$\Delta E^{\xi}_{\mathrm{HF}}(n_x) = \sum_{\xi'} (\tilde{W}_0^{\xi\xi'\xi'\xi} + \tilde{W}_0^{\xi\xi'\xi\xi'}) n_x^{\xi'} \ , \tag{4.6}$$

where $\tilde{W}_0^{\xi_1\xi_2\xi_3\xi_4} = \delta_{\xi_1,\xi_4}\delta_{\xi_2,\xi_3}\tilde{W}_0^{\xi_1\xi_2}$ with $\tilde{W}$ defined in Eq. (3.10) and n_x^{ξ} is the valley-specific exciton density. In contrast to the section above, we here include interactions between hybrid excitons in different valleys ξ and ξ' as we here want to consider a homobilayer in which generally several hybrid excitons with different layer hybridization and valley configurations are energetically favorable (cf. Section 3.4 and Fig. 3.4). We may express the energy renormalization in terms of an interaction dipole length, d^{ξ} according to $\Delta E^{\xi}_{\mathrm{HF}}(n_x) \sim d^{\xi}_{\mathrm{eff}} e_0^2 n_x/\epsilon$, where $n_x = \sum_{\xi} n_x^{\xi}$. This quantity directly determines the corresponding valley-specific energy renormalization for a single exciton. Furthermore, we define an average interaction-induced dipole length for the whole exciton gas as $d_{\mathrm{eff}} = \frac{1}{n_x}\sum_{\xi} d^{\xi} n_x^{\xi}$, which can be interpreted as a measure of the effective interaction strength in the system.

As the hybrid exciton-exciton interaction is highly electrically tunable (Section 3.4), it follows that also the interaction-induced dipole and energy renormalizations in a homobilayer can be substantially enhanced with out-of-plane electric fields, as is shown in Fig. 4.2(a). In particular, we find for the naturally stacked WSe_2 homobilayer, that the weak dipole-dipole interaction between KΛ and K'Λ' hybrid excitons (Fig. 3.5), is characterized by negligible interaction dipole lengths at vanishing electric fields. The transition between exciton ground states at elevated electric fields, from a mostly intralayer-like state to a mostly interlayer-like state (cf. Fig. 3.4(b) and Fig. 4.2(b)), is accompanied by a drastic increase of the effective dipole length. As such, we predict that substantial luminescence blue-shifts of the order of tens of meVs can be engineered by applying an electric field, $|E_z| > 0.15$ V/nm. In summary, we distinguish between two different regimes for interactions: a low-dipole regime at $|E_z| < 0.15$ V/nm involving weakly interacting hybrids and a high-dipole regime at $|E_z| > 0.15$ V/nm. The transition between the regimes is also tunable with temperature (cf. solid and dashed lines in Fig. 4.2), reflecting the interplay in relative occupations of intralayer-like and interlayer-like states at elevated temperatures.

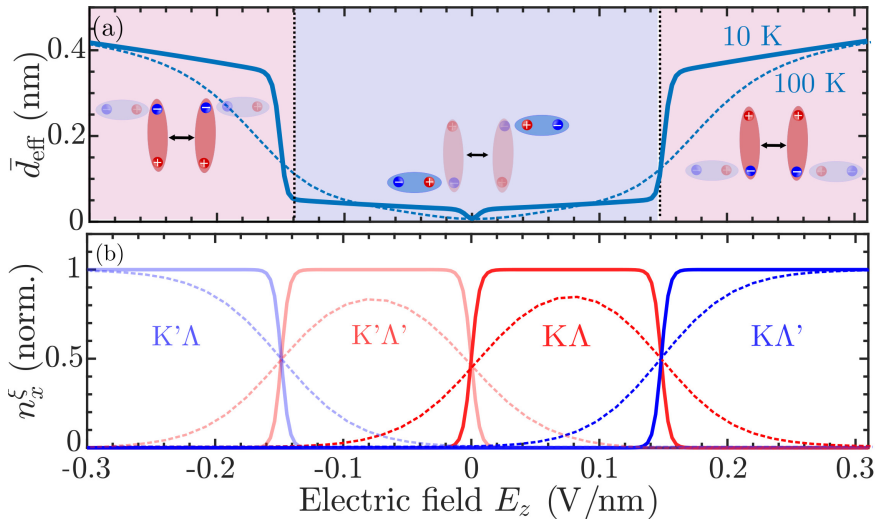

Figure 4.2: Interaction-induced dipole lengths in naturally stacked WSe_2 homobilayers. (a): Electrically tunable dipole lengths at T=10 K (solid lines) and T=100 K (dashed lines). (b): Valley-specific exciton occupations, revealing a transition from a mostly occupied intralayer-like state (red) to a mostly occupied interlayer-like (blue) state at elevated electric fields, E_z. Figure taken from Ref. [91] (Paper IV).

In Paper V, we show, by combining the microscopic theory outlined above and electric field- and power-dependent photoluminescence measurements carried out by the group of Andras Kis (EPFL), that electric fields indeed can be used to enhance excitonic non-linearities in optical spectra [92]. The repulsive interactions between dipolar excitons have also intriguing consequences for how excitons move in space and time as is shown in the next chapter.

5

Anomalous exciton transport

Being able to control and track excitons in space and time is crucial for the operation of TMD-based devices, such as excitonic transistors [111]. Excitons have shown to be remarkably mobile and can be efficiently guided by potential gradients [31, 50, 113, 114] and exhibit intriguing transport properties and unconventional diffusion [115–117]. Therefore, a lot of recent research on 2D materials has been focused on understanding the underlying interaction mechanisms governing exciton transport. In this chapter, we shed light on the key role of electron-hole density in exciton propagation in van der Waals heterostructures. It is shown that dipole-dipole repulsion between interlayer excitons give rise to non-linear, so-called anomalous, exciton transport. Moreover, the tuning of interlayer exciton transport with layer separation is emphasized. Finally, we reveal that hybrid exciton transport can be efficiently controlled with out-of-plane electric fields. Our findings on interlayer exciton transport are reported in Paper III and hybrid exciton transport is investigated in Paper IV and in a joint experiment-theory study, Paper V. In the following, we summarize the most important insights on exciton transport as obtained in Paper III-V.

Obtaining a thorough microscopic understanding of exciton transport across a wide range of densities of electrons and holes remains challenging due to the complex interplay between free and bound charge complexes [34]. However, here we focus on excitation regimes in which excitons stay bound and dom-

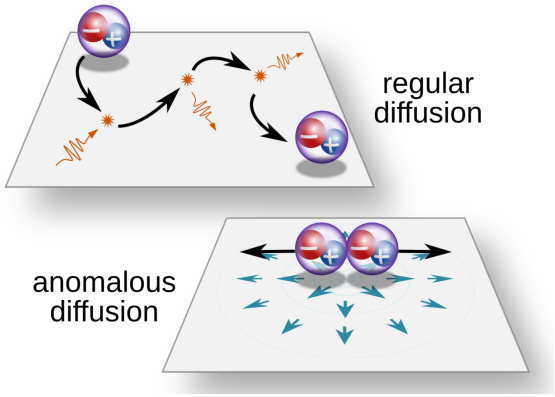

Figure 5.1: Exciton diffusion in atomically thin semiconductors. In the intermediate excitation regime, exciton transport is characterized by regular diffusion and is governed by exciton-phonon scattering. At high densities, exciton transport can be governed by exciton-exciton repulsion. The repulsion between excitons gives rise to a drift force pushing excitons away from the excitation spot resulting in anomalous diffusion. Figure adapted from Ref. [11] (Paper VIII).

inate the optical response, i.e. at densities $n_x \approx 10^{10} - 10^{13}$ cm^{-2} [112]. At intermediate electron-hole densities ($n_x \lessapprox 10^{11}$ cm^{-2}), exciton propagation is governed by the scattering with phonons, and is referred to as conventional or regular diffusion [118]. However, at larger densities, exciton-exciton interactions become important resulting in anomalous diffusion, cf. Fig. 5.1. In TMD monolayers, the observed non-linear exciton transport has been ascribed to efficient Auger scattering[1] [115, 116], but in bilayers anomalous diffusion is often a result of strong dipole-dipole repulsion between interlayer excitons as evidenced by recent experiments [33, 52, 92]. Guided by these experiments and our microscopic theory on exciton-exciton interactions developed in previous chapters, we are almost set for investigating exciton transport at elevated densities in van der Waals heterostructures. First, we need to extend the theoretical framework introduced in previous chapters to excitons propagating in both space and time, i.e. resolve their spatiotemporal dynamics.

[1]Auger scattering or exciton-exciton annihilation in monolayers is discussed in the following chapter. Here, we focus on homobilayers and specific TMD heterostructures in which Auger processes are seen to be less efficient [119].

5.1 Drift-diffusion equation and spatiotemporal dynamics

In order to microscopically access the spatiotemporal dynamics of excitons, we turn to Wigner function formalism [120]. In this formalism, we gain information about the spatial and temporal dependence via the Wigner function $N_{\mathbf{Q}}(\mathbf{r}) = \sum_{\mathbf{q}} \mathrm{e}^{i\mathbf{q}\cdot\mathbf{r}} \langle X^{\dagger}_{\mathbf{Q}-\mathbf{q}/2} X_{\mathbf{Q}+\mathbf{q}/2} \rangle$, which is the quasiprobability distribution of excitons with center-of-mass momentum $\mathbf{Q}$ at position $\mathbf{r}$ [115]. Here, $X^{(\dagger)}$ are excitonic operators, as introduced in Section 2.5. As outlined in detail in Ref. [120] for carriers, the spatiotemporal dynamics can be accessed by evaluating the Heisenberg equation of motion for the off-diagonal quantity $N_{\mathbf{Q},\mathbf{Q}'} \equiv \langle X^{\dagger}_{\mathbf{Q}} X_{\mathbf{Q}'} \rangle$ and Fourier-transform the result to get an equation of motion for the Wigner function [115, 118]. To take exciton-exciton interactions into account we make use of the excitonic Hamiltonian in Eq. (3.1), which together with the free exciton Hamiltonian (2.27) gives the equation of motion for $N_{\mathbf{Q},\mathbf{Q}'}$. By Fourier transforming and performing a Taylor expansion with respect to momentum and space coordinates, the following equation of motion is found

$$\dot{N}_{\mathbf{Q}}(\mathbf{r},t) = -v_{\mathbf{Q}} \nabla_{\mathbf{r}} N_{\mathbf{Q}}(\mathbf{r},t) - \frac{v_{\mathbf{Q}}}{k_B T} \cdot \nabla_{\mathbf{r}} (\Delta E(n)) N_{\mathbf{Q}}(\mathbf{r},t)(1 + N_{\mathbf{Q}}(\mathbf{r},t)) \ . \quad (5.1)$$

Here, the first term describes free propagation of excitons with velocity $v_{\mathbf{Q}} = \frac{\hbar \mathbf{Q}}{M}$, M being the total exciton mass. The second term results in a drift of excitons due to their mutual interaction which enters via the now space- and time-dependent energy renormalization ΔE, obtained by promoting $n_x \to n(\mathbf{r},t)$ in Eq. (4.3). It was here assumed that the momentum dependence in $N_{\mathbf{Q}}(\mathbf{r},t)$ is given by an equilibrium Bose distribution with temperature T. Next, we recognize the equation above as a Boltzmann transport equation. By including also collision terms due to e.g. exciton-phonon scattering, invoking the relaxation time approximation and making use of the continuity equation (details spelled out in [120]) we obtain an equation of motion for the space- and time-dependent exciton density

$$\partial_t n(\mathbf{r},t) = \nabla_{\mathbf{r}} \cdot (D(n) \nabla_{\mathbf{r}} n(\mathbf{r},t)) + \mu_m \nabla_{\mathbf{r}} \cdot [\nabla_{\mathbf{r}} (\Delta E(n)) n(\mathbf{r},t)] - \frac{n(\mathbf{r},t)}{\tau} \ , \quad (5.2)$$

with $n(\mathbf{r},t) = \sum_{\mathbf{Q}} N_{\mathbf{Q}}(\mathbf{r},t)$. Here, we introduced the diffusion coefficient $D = D_0 \frac{T_d}{T}[\exp(T_d/T) - 1]^{-1}$, D_0 being the low-density diffusion coefficient[2], $T_d = \frac{2\pi\hbar^2 n}{k_B M}$ is the degeneracy temperature and $\mu_m = \frac{D_0}{k_B T}$ is the exciton mobility, following the Einstein relation. We also phenomenologically took into account the radiative decay of excitons by including a term proportional to $1/\tau$, τ being the life time.

Eq. (5.2) is commonly referred to as a drift-diffusion equation [121], with the first term describing the free propagation of excitons and the second term denoting the Coulomb-induced drift term, which at high densities is responsible for anomalous diffusion (Fig. 5.1). In fact, the derived drift-diffusion is very general and could be extended to include potential gradients due to e.g. inhomogenous strain, or gating [83,111,122]. The solution to (5.2) provides access to the space- and time-dependent exciton density and allows us to investigate the impact of exciton-exciton interactions on non-linear exciton transport further. In the following, we apply our material-specific theory to investigate interlayer exciton transport in a TMD heterobilayer and hybrid exciton transport in a homobilayer at elevated densities.[3]

5.2 Interlayer exciton transport

Here, we briefly summarize our theoretical findings on interlayer exciton transport in an hBN-encapsulated $MoSe_2$-hBN-WSe_2 heterostructure as considered in a recent experiment [52]. In Fig. 5.2 we present the spatiotemporal dynamics of interlayer excitons obtained from solving Eq. (5.2). We initialize the exciton density as a Gaussian distribution, such that $n(x,y) = n_x \exp[-(x^2 + y^2)/\sigma^2(0)]$ with the initial peak density $n_x = 5 \cdot 10^{12}$ cm^{-2} and variance (laser spot size) $\sigma^2(0) = 1$ μm^2. As time progresses the initial distribution develops into a super-Gaussian as illustrated in Fig. 5.2(a). In-

[2]The diffusion coefficient, D_0, is determined by exciton-phonon scattering rates which can be microscopically calculated, see e.g. Ref. [115, 118]. In this work and Paper III-V, we however adapt the diffusion coefficient from experimental measurements [52, 92].

[3]Exciton transport in TMD monolayers has already been extensively studied for a broad range of densities [32, 113, 115, 116, 123]. In particular, it has been shown that monolayers exhibit intriguing unconventional diffusion characterized by spatial rings, i.e. exciton halos, in the high excitation regime, at room temperature.

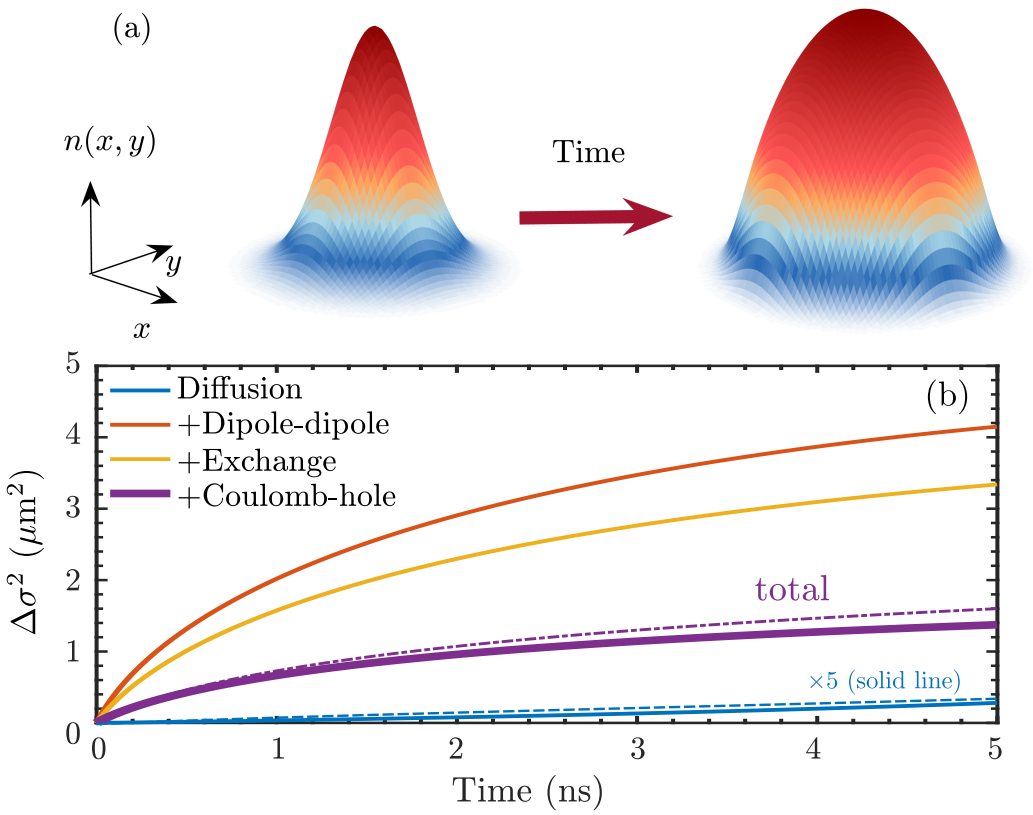

Figure 5.2: Exciton transport in $MoSe_2$-hBN-WSe_2 heterostructures. (a) Time evolution of exciton density $n(x,y,t)$, assuming a Gaussian distribution at $t = 0$. (b) Time-dependent spatial broadening, separating contributions from diffusion (blue) and different drift terms. Note that the contributions are consequtively added up. The dashed lines show the solution of the drift-diffusion equation assuming a Boltzmann distribution for the interlayer exciton. Figure adapted from Ref. [90] (Paper III).

cluding, only diffusion, i.e. the first term in (5.2), we note that variance of the distribution (Fig. 5.2(b)), i.e. the spatial broadening $\Delta\sigma^2 = \sigma^2(t) - \sigma^2(0)$, acquires a sublinear time-dependence (solid blue lines). This is a result of efficient boson bunching, which is prominent at the very high considered densities. In contrast, taking the diffusion coefficient as density-independent corresponding to considering a Boltzmann distribution as initial distribution for the excitons (dashed lines), we retain Fick's law, i.e. a variance which varies linearly with respect to time. However, including also exciton-exciton

interactions, we deduce that the exciton transport is boosted and displays a non-linear time dependence - a hallmark of anomalous diffusion. As the repulsive exciton-exciton interactions is weakly reduced by exchange interactions (as a consequence of its net attractive nature for interlayer excitons, cf. Eq. (4.5) and the discussion in Section 4.1) and exciton screening, the anomalous diffusion becomes less enhanced when including all Coulomb-induced contributions to the drift term. Finally, we note that the non-linear character of the interlayer exciton transport can be tuned by changing the (initial) electron-hole density n_x. As shown in Paper III, electron-hole densities $n_x > 10^{12}$ cm^{-2} are needed in order for Coulomb-induced drift to dominate over purely diffusive propagation.

As discussed already in the previous chapter, the strong dipole-dipole repulsion between interlayer excitons is directly proportional to the spatial separation between the electron and hole forming the interlayer exciton (Eq. (4.4)). This implies that the exciton-exciton interaction is highly tunable with layer separation and the interaction strength in van der Waals heterostructures can be experimentally controlled simply by including dielectric spacers between the stacked TMD monolayers. In particular, to lowest order in momentum, it can be shown, by generalizing the Keldysh screening for excitons, that the inclusion of a dielectric spacer (e.g. hBN spacer) of thickness d_{hBN} and dielectric constant κ_{hBN} modifies the dipole-dipole interaction as $g_{d-d} \sim \frac{d_{\mathrm{TMD}}}{\varepsilon_{\mathrm{TMD}}} + \frac{d_{\mathrm{hBN}}}{\kappa_{\mathrm{hBN}}}$. We have, in fact, already been considering a heterotrilayer in the transport study above, with a single hBN spacer ($d_{\mathrm{hBN}} = 0.3$ nm) acting as a dielectric[4] between molybdenum- and tungsten-layers.

In Fig. 5.3, we show the time-dependent effective diffusion coefficient given by the slope[5] of the variance, i.e. $D_{\mathrm{eff}}(t) \equiv \frac{1}{4}\frac{d}{dt}\sigma^2(t)$ for different number of hBN spacers between the TMD layers. For small times t, the obtained effective diffusion coefficient can differ more than an order of magnitude from the low density diffusion coefficient D_0 (indicated with an orange dashed line). This reflects the overall faster propagation of interlayer excitons at elevated

[4]The inclusion of a hBN spacer between the TMD layers does not only enhance the dipole moment of interlayer excitons, but also suppresses the impact of moiré potentials which may trap excitons and affect their transport properties [83, 124].

[5]In the low density regime, where diffusion dominates over repulsive exciton-exciton interactions, Eq. (5.2) can be solved analytically and the time-dependent two-dimensional variance is given by $\Delta\sigma^2 = 4D_0t$.

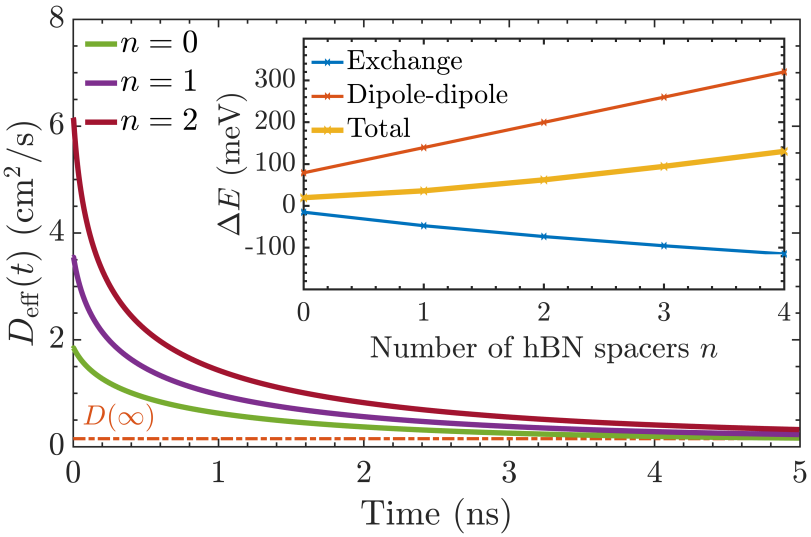

Figure 5.3: Time-dependent effective diffusion coefficient for different number of hBN spacers, n. The inset illustrates the dependence of the interlayer separation, $R = nd_{\mathrm{single,hBN}}$, $d_{\mathrm{single,hBN}} = 0.3$ nm on the exciton-exciton interaction, revealing a net increase of the interaction with layer separation. Figure taken from Ref. [90] (Paper III).

electron-hole densities and the importance of the interlayer exciton drift (cf. Eq. (5.2)). When increasing the number of hBN spacers between the layers, anomalous diffusion is enhanced as a consequence of increased dipole moments of interlayer excitons with layer separation (cf. inset in Fig. 5.3). Intriguingly, we also find that the exchange interactions become more attractive as the number of hBN spacers increases, counteracting the repulsive dipole-dipole interaction. This can be explained by the interplay of different Coulomb matrix elements entering Eq. (4.5) and their dependence on dielectric environment, cf. Paper III for details. As time progresses, excitons drift away from the initial laser spot and exciton density drops, and eventually conventional diffusion starts to dominate over Coulomb-induced drift, causing the effective diffusion coefficient to coincide with the low density diffusion coefficient $D_0 = 0.15$ cm^2/s at $t \to \infty$.

By tuning the layer separation between TMD layers we have hence shown how the non-linear character of the interlayer exciton transport can be experimentally controlled. In Paper III, we also study alternative tuning knobs

of exciton transport such as the surrounding substrate of heterostructure, as well as the size of laser spot size.

The initial study on exciton transport discussed above paves the way for investigating more complex material systems such as twisted moiré structures where excitons can be trapped efficiently by strong moiré potentials [33,83] or homobilayers where the dominating exciton species are layer-hybridized [125]. In the following, we return to the WSe_2 homobilayers considered in Sections 3.4 and 4.2 and in Paper IV-V and discuss the remarkable electrical tunability of hybrid exciton transport.

5.3 Electrical control of hybrid exciton transport

In previous chapters, it was shown that layer-hybridized excitons couple efficiently to electric fields via their interlayer component and out-of-plane dipole moment. It was moreover revealed that dipolar interactions betweeen hybrid excitons are electrically tunable and demonstrated the emergence of two intriguing interaction regimes in WSe_2 homobilayers as function of electric field. As is shown in Paper IV, hybrid exciton transport can be modeled using a drift-diffusion equation analogous to (5.2) but with a drift term which is dictated by an average energy renormalization $\Delta\bar{E}(n) = \frac{\bar{d}_{\text{eff}} e_0^2}{\epsilon_0 \epsilon_{\text{TMD}}^{\perp}} n(\mathbf{r},t)$ for the entire exciton gas, where $\bar{d}_{\text{eff}}$ is found from averaging over valley-specific interaction-induced dipole lengths obtained from Eq. (4.6). As such, the two interaction regimes appearing at small and elevated electric fields are expected to also be reflected in field-dependent studies of the spatiotemporal dynamics of hybrid excitons.

In Fig. 5.4, the spatial broadening of the hybrid exciton distribution as a function of time and electric field is shown. Here, we assumed an initial hybrid exciton density $n_x = 10^{12}$ cm^{-2} and do not take into account correlation or screening effects which could yield quantitative corrections to the obtained broadenings. Furthermore, we stay in a density regime in which the initial exciton distribution can be treated as Boltzmannian and the diffusion coef-

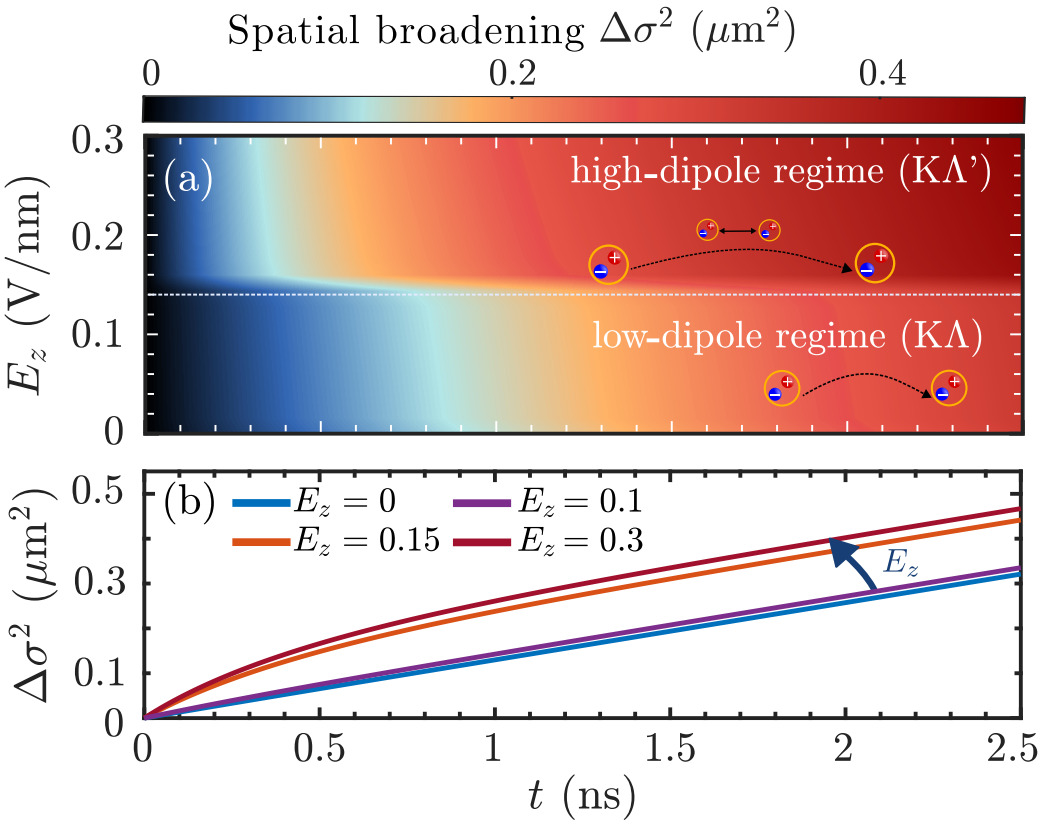

Figure 5.4: Hybrid exciton transport in WSe_2 homobilayers. (a): Electric field- and time-dependent spatial broadening of exciton distribution reveals conventional and anomalous exciton diffusion in low-dipole and high-dipole interaction regimes, respectively. (b): Spatial broadening as a function of time at fixed out-of-plane electric fields, E_z. Figure adapted from Ref. [91] (Paper IV).

ficient $D(n) = D_0$ (cf. Eq. (5.2)). In Fig. 5.4(a), we identify two crucially different regimes for exciton transport. At low electric fields, $E_z < 0.15$ V/nm, weakly interacting and mostly intralayer-like KΛ excitons give rise to linear exciton transport with a spatial broadening $\Delta\sigma^2(t) \sim D_0 t$ [118]. At larger electric fields, $E_z > 0$, the transport is rendered from linear to anomalous propagation, reflecting the strong repulsive interactions between dominant KΛ' excitons at these fields (cf. Fig. 3.4(d) and Fig. 4.2). At time-scales $t \gtrsim 1$ ns, the density of excitons has dropped significantly, and the diffusion becomes linear again also at elevated electric fields. The transition from the low-dipole regime to the high-dipole is accompanied by nearly

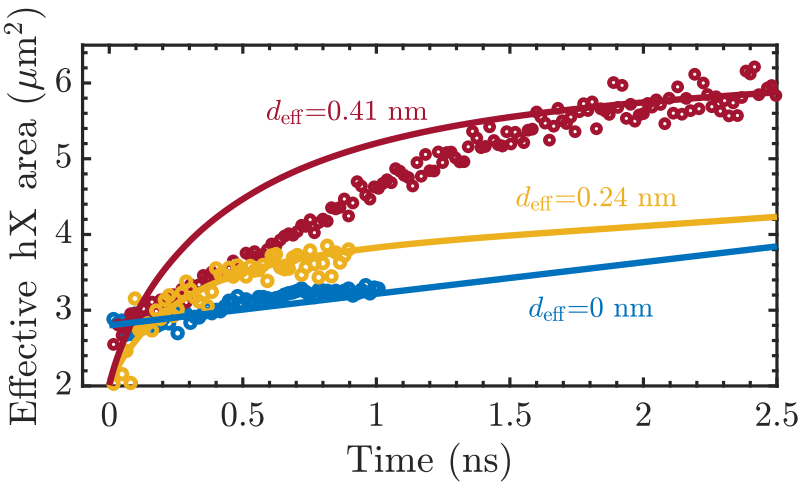

Figure 5.5: Hybrid exciton transport in WSe_2 homobilayers. Experiment (dotted lines) and theory (solid lines) reveal a strongly dipole-dependent exciton transport in the high-excitation regime ($n_x \sim 10^{12}$ cm^{-12}). Figure adapted from Ref. [92] (Paper V).

a two-fold increase in diffusion lengths, cf. Paper IV.

The strongly electric-field-dependent hybrid exciton transport has also been confirmed by spatiotemporal measurements performed by the group of Andras Kis (EPFL) as reported in Paper V and Fig. 5.5. In this work, we use the experimentally extracted dipole lengths obtained from field-dependent photoluminescence measurements at high power as input for the drift-diffusion equation in order to make a consistent comparison between experiment and theory. The dipole lengths are extracted at three different electric fields, $E_z = 0, \pm 0.3$ V/nm and obtained as $d_{\text{eff}}(E_z = 0) \sim 0$, $d_{\text{eff}}(E_z = 0.3\ \text{V/nm}) = 0.41$ nm and $d_{\text{eff}}(E_z = -0.3\ \text{V/nm}) = 0.24$ nm and are in good agreement with microscopically calculated dipole lengths, cf. Fig. 4.2.[6] Furthermore, we here consider the expansion of the hybrid exciton cloud as a function of time, by introducing the effective hybrid exciton area $A(t) = \pi x_0^2(t)$ where the radial broadening $x_0^2(t)$ is extracted from the threshold condition $n(x_0, 0, t)/\max(n(x_0, 0, t)) = 1/e$ for fixed times t, $n(x,y,t)$ being the

[6]The asymmetry in the magnitude of the experimentally extracted dipole lengths for positive and negative electric fields is not present in our microscopic theory, but is believed to be due to intrinsic doping [92].

space- and time-dependent exciton density. In this way, the expansion of the exciton cloud is consistently obtained between simulations and experiments. Importantly, at vanishing and small electric fields, the exciton cloud can be fitted with a linear function with respect to time even at high density (solid blue line), indicating that exciton-exciton interactions are weak in this regime - consistent with our microscopic theory. Instead, at elevated electric fields (red and yellow lines) anomalous and non-linear diffusion is clearly observed as predicted from theory (Fig. 5.4). Overall, our joint experiment-theory study shows that the hybrid exciton transport is highly tunable with electric fields and dipolar interactions can be efficiently controlled in WSe_2 homobilayers. In particular, the remarkable electrical tunability of the repulsion between dipolar excitons could further potentially be exploited to engineer exotic phases of matter such as Bose-Einstein condensates of excitons, of which there have been recent indications in the considered bilayer structure [126].

6

Auger-like exciton recombination

In this chapter, we will be concerned with a particularly important scattering process which fundamentally limits the efficiency of optoelectronic applications, referred to as exciton-exciton annihilation. This type of non-radiative recombination process determines life-times and transport properties of excitons in TMD monolayers at elevated densities [115,116,119]. Exciton-exciton annihilation (EEA) involves, as the name suggests, two excitons which, if the density is sufficiently high and resonance conditions are fulfilled, could annihilate each other and form a higher-energetic exciton (HX), as schematically illustrated in Fig. 6.1 (a). This implies that, in contrast to the scattering processes discussed in Chapter 3 and in Paper I, we here consider Auger-like processes involving three different carriers.

Auger scattering has previously been shown to be extremely efficient in e.g. graphene [127]. In graphene, the traditional Auger recombination process takes place when an electron in the conduction band recombines with a valence band electron and another conduction band electron is excited further up into the same conduction band. Transition-metal dichalcogenides have a finite band gap and exhibit a richer band structure than graphene containing multiple bands and valleys and allow for additional scattering channels for Auger recombination. In particular, considering tungsten-based monolayers, which have a dark excitonic ground state (cf. Fig. 2.3) [128], we may distinguish between intravalley Auger recombination processes (I) and intervalley processes (II and III), cf. Fig. 6.1(b). Furthermore, due to the favorable

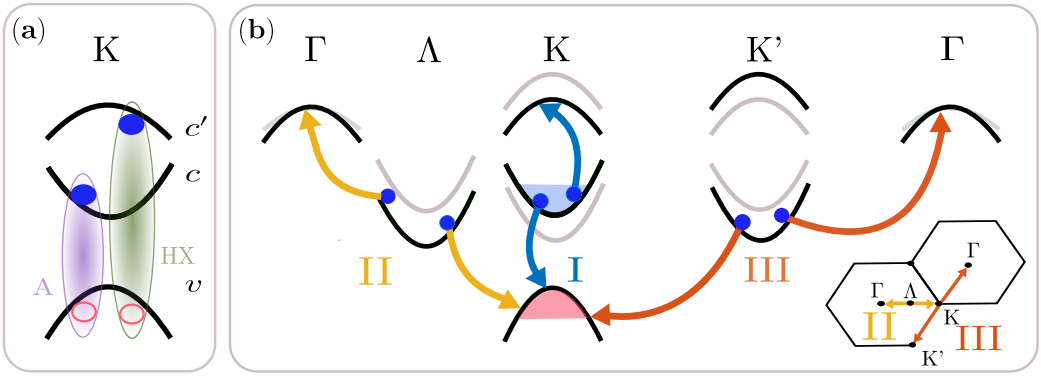

Figure 6.1: Schematic illustration of exciton-exciton annihilation processes in monolayer WSe_2. (a) The annihilation of two A excitons (purple) gives rise to a higher-lying HX exciton (green). (b) We distinguish between three different Auger scattering processes: intravalley processes (I, blue) between KK excitons resulting in a final higher-lying KK exciton state, intervalley processes involving scattering between KΛ (II, yellow) or KK' (III, red) excitons where the final state is a KΓ exciton. Figure is adapted from Ref. [133] (Paper II).

energetic separation of conduction bands and the fact that the conduction and valence bands exhibit a parabolic dispersion around the high-symmetry points in these particular materials it turns out that Auger recombination processes involving two different conduction bands[1] [132], as shown in Fig. 6.1, are possible and, as we show in Paper II, highly efficient.

In the following, we briefly summarize the findings in Paper II by introducing the theoretical framework for exciton-exciton annihilation and use it to evaluate the exciton-exciton annihilation rate or Auger coefficient, which is an experimentally accessible quantity. The microscopic and material-specific theory presented in this chapter has been supported and successfully confirmed by time-resolved photoluminescence measurements carried out by the group of Alexey Chernikov (TU Dresden).

[1]The higher-lying conduction bands which make the scattering processes most resonant are negatively curved. This puts a constraint on the reduced exciton mass to be positive and for the final exciton state to be bound such that $|m_e| > |m_h|$. This condition holds for our final states, and the existence of higher-lying exciton states has recently been established in monolayer and bilayer WSe_2 experimentally through up-converted photoluminescence measurements [129–131].

6.1 Excitonic Auger Hamiltonian

We address exciton-exciton annihilation in TMD monolayers by starting off from the electronic multivalley and three-band electronic Hamiltonian

$$H_{\mathrm{Aug}} = \sum_{\substack{\mathbf{k}_1,\mathbf{k}_2,\mathbf{q} \\ \xi_1 \ldots \xi_4}} V^{\xi_1\xi_2\xi_3\xi_4}_{\mathrm{Aug},\mathbf{q}} a^\dagger_{c',\xi_1,\mathbf{k}_1+\mathbf{q}} a^\dagger_{v,\xi_2,\mathbf{k}_2-\mathbf{q}} a_{c,\xi_3,\mathbf{k}_2} a_{c,\xi_4,\mathbf{k}_1} + \mathrm{h.c.} \tag{6.1}$$

Here, $V^{\xi_1..\xi_4}_{\mathrm{Aug},\mathbf{q}}$ is the electronic Auger matrix element determining the probability of scattering between different conduction bands $c^{(\prime)}$ and valence bands v in valleys $\xi_1 ... \xi_4$ with a momentum transfer $\mathbf{q}$. In this matrix element, the optical matrix element, M, crucially enters, providing the transition probability of scattering between different conduction bands or between conduction and valence bands (second part in Eq. (2.8)). The optical matrix elements depend strongly on electronic wave function overlaps and have been extracted from *ab-initio* calculations, performed by Roland Gillen, Friedrich-Alexander Universität, Erlangen-Nuremberg.

We now proceed to find the excitonic analogue of (6.1). In this work, this is done by carrying out the three following steps (in analogy to how the exciton-exciton interaction was found in Papers III-IV, cf. Chapter 3): **i)** compute the equation of motion for the microscopic polarization using (6.1), **ii)** transform the resulting equation to the exciton basis and **iii)** define an excitonic Hamiltonian of the form $H_{x,\mathrm{Aug}} = \sum_{\mu,\nu,\rho,\mathbf{Q},\mathbf{Q}'} V^{\mu\nu\rho}_{\mathbf{Q},\mathbf{Q}'} Y^\dagger_{\mu,\mathbf{Q}+\mathbf{Q}'} X_{\nu,\mathbf{Q}} X_{\rho,\mathbf{Q}'}$, where $Y^\dagger$ creates a higher-lying exciton composed by an electron from the higher-lying conduction band c' and valence band v and X annihilates two conventional excitons, cf. Fig. 6.1(a). The excitonic Auger matrix element $V^{\mu\nu\rho}_{\mathbf{Q},\mathbf{Q}'}$ is then obtained by requring bosonic commutator relations for the excitonic operators, deriving the corresponding equation of motion directly in the exciton picture and comparing the result with the equation from step **ii)**. The steps are carefully laid out in the Supplementary Material of Paper II and the excitonic Auger matrix elements can be found there-in. Here, we just note that, besides being directly dependent on the electronic Auger interaction, the excitonic matrix elements also depend on excitonic wave function overlaps between higher-lying and conventional excitons. In summary, we find the following excitonic Hamiltonian describing exciton-exciton annihila-

tion

$$H_{x,\mathrm{Aug}} = \frac{1}{2} \sum_{\mu,\nu,\rho,\mathbf{Q},\mathbf{Q}'} V^{\mu\nu\rho}_{\mathbf{Q},\mathbf{Q}'} Y^{\dagger}_{\mu,\mathbf{Q}+\mathbf{Q}'} X_{\nu,\mathbf{Q}} X_{\rho,\mathbf{Q}'} + \mathrm{h.c.}\ . \tag{6.2}$$

Here, the excitonic indices μ, ν, ρ are compound indices which carry both the exciton valley and state. In particular, we fix the initial exciton states to be $1s$ exciton states as these states are mostly occupied, but include $1s$, $2s$ and $3s$ states as final (HX) states. The excitonic Auger matrix element decays rapidly with final exciton state due to the shrinking overlap with the initial $1s$ states, as shown in Paper II, such that it suffices to only include higher-lying excitons with low quantum numbers in our calculations.

6.2 Temperature-dependent Auger recombination rates

Exciton-exciton annihilation is experimentally addressed by means of time-resolved photoluminescence (TRPL) measurements and via the exciton-exciton annihilation rate or Auger coefficient, R_A. Time-resolved photoluminescence spectra provide information about how the exciton population decays with time for a given excitation power. In particular, EEA is seen to lead to an effective saturation of the exciton density at high excitation powers [134]. Here, we get microscopic access to the Auger coefficient by considering the Heisenberg equation of motion for the initial density of A excitons, $n_x = \sum_{\nu\mathbf{Q}} N^{\nu}_{A,\mathbf{Q}}$, reading $\dot{n}_x = -R_A n_x^2$. We find[2] that the Auger coefficient reads

$$R_A = \frac{2\pi}{\hbar} \sum_{\mu,\nu,\rho,\mathbf{Q},\mathbf{Q}'} |V^{\mu\nu\rho}_{\mathbf{Q},\mathbf{Q}'}|^2 N^{\nu}_{A,\mathbf{Q}} N^{\rho}_{A,\mathbf{Q}'} \delta(\Delta\epsilon)\ , \tag{6.3}$$

where $\Delta\epsilon$ expresses energy conservation between initial (A) and final (HX) exciton states in the scattering process and includes differences in HX and A exciton center-of-mass dispersions (Eq. (2.27)) and single-particle energy

[2]In deriving the exciton-exciton annihilation rate we applied the second order Born-Markov approximation, an approximation frequently used when treating many-body scattering processes. Within this approximation, non-linearities caused by quantum memory effects are neglected such that adiabatic solutions which express energy-conserving processes are obtained [105].

separations such as spin-orbit and valley splittings. Furthermore, we estimate the appearing A exciton occupations $N^{\nu}_{A,\mathbf{Q}}$ with Boltzmann distributions, resulting in an explicitly temperature-dependent Auger coefficient. In Figure

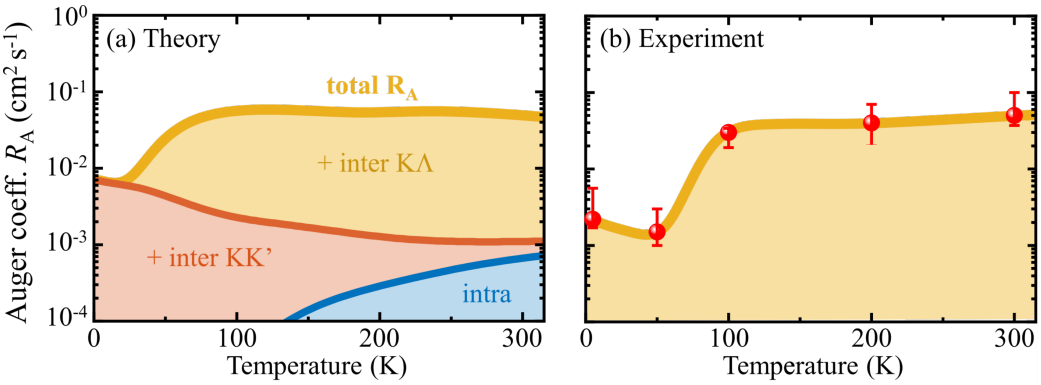

Figure 6.2: Temperature-dependent Auger coefficients in hBN-encapsulated monolayer WSe_2. (a) Calculated Auger coefficient separating contributions from intra- and intervalley processes, revealing the crucial importance of intervalley KΛ-KΛ scattering channels at room temperature. (b) Temperature-dependent Auger coefficients as extracted from time-resolved photoluminescence measurements. Figure adapted from Ref. [133] (Paper II).

6.2(a), we present the calculated Auger coefficient for an hBN-encapsulated WSe_2 monolayer. Importantly, we reveal a highly non-monotonous dependence with respect to temperature. This temperature dependence is explained through the interplay of KK', KΛ and KK A exciton occupations at different temperatures and reflects well the temperature dependence of valley-specific densities, $n^{\nu}_{x}(T) = \sum_{\mathbf{Q}} N^{\nu}_{A,\mathbf{Q}}(T)$, as obtained by the Boltzmann distribution. Furthermore, we have separated contributions stemming from intravalley Auger processes (process I in Fig. 6.1 (b)) and intervalley Auger recombination (processes II and III in Fig. 6.1 (b)). Crucially, we find that the impact of intravalley processes on the EEA is negligible, reflecting the low occupation of KK excitons at all temperatures. At low temperatures, the dark scattering channel involving KK' excitons is dominant, as these exciton states are the predominantly occupied states at these temperatures. At elevated temperatures, the dark intervalley KΛ scattering channel becomes highly efficient. This is due to two reasons: **i**) a predominant occupation of KΛ excitons at room temperature, being a consequence of the three-fold degeneracy of the Λ valley and energetic ordering of bright and dark exciton

states in WSe_2 (Fig. 2.3(b)) [39], **ii)** optimal energy separations and resonance conditions for the scattering to occur (given by $\Delta\epsilon$ in (6.3)). Note that the size of the excitonic Auger matrix element of the KΛ channel relative to the KK channel plays a minor role for the scattering efficiency, despite the large momentum transfer entering and suppressing the KΛ matrix element.

In Fig. 6.2 (b) we present the Auger coefficients as extracted from time- and temperature-resolved photoluminescence measurements conducted by the group of Alexey Chernikov (TU Dresden). We find an excellent agreement between theory and experiment - clearly revealing the impact of dark Auger recombination processes in the exciton-exciton annihilation in WSe_2. Hence, remarkably, this joint theory-experiment study shows that momentum-dark excitons, although not being directly accessible by light, can contribute to the efficiency of exciton-based devices as efficient Auger recombination rates are seen to fundamentally lead to a saturation of exciton densities. Finally, we note that our material-specific theory can be used to study the dependence of the dielectric environment on the EEA rates. In Paper II, we show that, by changing the dielectric constant of the material surrounding the TMD, the resonance conditions for efficient EEA also change owing to the sensitive dependence of screening on the exciton energy landscape. Overall, this work provides experimentally and technologically viable pathways to tune and design inelastic many-body interactions in nanostructured systems.

7 Conclusion and outlook

In this thesis, we shed light on the fundamental interaction mechanisms between excitons in atomically thin semiconductors. In our work, which is based on a material-specific and quantum-mechanical many-particle theory, the crucial impact of exciton-exciton interactions on exciton optics, dynamics and transport in two-dimensional transition-metal dichalcogenide mono- and bilayers is emphasized. In particular, we show that excitons in TMD monolayers exhibit significant exchange interactions between carriers reflecting their fermionic substructure and that spatially separated interlayer excitons interact via strong dipole-dipole repulsion. The latter gives rise to experimentally observed blue-shifts in optical spectra and non-linearities in interlayer exciton transport in the form of anomalous diffusion. Furthermore, the theoretical framework was extended to layer-hybridized excitons with the main outcome that the dipolar interaction between these quasiparticles is highly tunable with respect to electric fields. The high electrical tunability of hybrid exciton-exciton interactions is also shown, by combining spatiotemporal measurements and microscopic theory, to result in an exciton transport behavior which can be electrically controlled. Finally, we provide a microscopic theory of exciton-exciton annihilation, i.e. an Auger-like recombination process, which is seen to limit the performance of photodetectors and solar cells based on 2D materials. Overall, our insights on exciton-exciton interactions could guide future experiments performed in the high excitation regime, contribute to the realization of optoelectronic TMD-based devices and, perhaps most intriguingly, be used to study other exotic quantum phases of matter.

In the following, some prospects for future research and possible extensions of the theoretical framework are provided.

The research focus of the 2D materials community has changed rapidly over the last decade. Considering just transition-metal dichalcogenides, these materials when e.g. integrated in optical cavities [135,136], vertically [53] or laterally stacked [137–139] have shown to exhibit remarkable correlated physics which goes well beyond the exciton physics in a single TMD monolayer. These material systems hold prospects for studying intriguing many-body interactions between more exotic quasiparticles, including exciton-polaritons which emerge as a result of the coupling between electron-hole pairs and light when TMDs are put in cavities, or one-dimensional charge transfer excitons forming at the interface of lateral heterostructures. The latter exhibit huge dipole lengths owing to the large spatial separation between electrons and holes, facilitating extremely long-range dipole-dipole repulsion [138,140]. The theoretical framework outlined in this thesis, in fact, allows for studying polariton-polariton interactions [110, 141, 142] as shown in an initial study (Paper IX) and could also provide the basis for investigating interaction-induced phenomena such as the Tonks-Girardeau phase of 1D charge transfer excitons in lateral structures [143, 144].

Finally, having focused on either monolayers or bilayers with a small difference in the lattice constants of the individual monolayers in this thesis, we turn to moiré materials and comment on the role of interactions in such structures. Moiré materials, obtained by stacking e.g. TMD layers on top of each other at a relative angle or by vertically stacking layers with substantially different lattice constants, have been extensively studied recently owing to their remarkable unconventional electronic properties which are a result of a strong moiré potential induced by the lattice [145]. The moiré potential provides a potential landscape in which quasiparticles can be efficiently trapped at different moiré sites [146–148] or individual charges can be separated [149]. The interplay between the moiré potential and the Coulomb interaction, or exciton-exciton interaction, has shown to give rise to a number of intriguing fermionic and bosonic phases of matter such as generalized Wigner crystal states of electrons [46, 47, 49, 150, 151] and superfluidity of excitons [152, 153], respectively. In an initial study on exciton-exciton inter-

actions in moiré structures [154], which takes the theory developed here as a starting-point, it has further been demonstrated that dipole-dipole repulsion between excitons in a moiré potential leads to a bosonic delocalization of interlayer excitons across the moiré lattice. Effectively, the dipole-dipole repulsion makes the moiré potential shallower and increases the probability for excitons to jump between different moiré sites. As such, exciton-exciton interactions could crucially influence the transport properties of excitons in twisted TMD bilayers. In future work, we would like to continue exploring strongly correlated physics in quantum materials. Given the plethora of fascinating many-body correlations that have been recently predicted just in TMD-based structures alone ranging from excitons of crucial importance for light emission and absorption to topological edge states of potential use for quantum computation [155, 156], it is probably justified to say that 2D materials remain at the heart of material science.

Acknowledgments

Here, I would like to distribute my gratitude to those who directly or indirectly contributed to the work summarized in this thesis. First, and above all, I would like to thank my supervisor **Ermin Malic**. I am so grateful for all your support, feedback, expertise and kind advice on how to navigate the sometimes rough waters of Academia. I can only summarize your supervision over the years in one word: *excellent*.

Secondly, I thank **Samuel Brem**. Your constant support during the early stages of my PhD studies was crucial for me. Besides contributing with many brilliant insights in my work, your determination has inspired and helped me gaining my confidence as a researcher.

I must also single out a big thank you to **Raul Perea-Causin** for constantly keeping your door open for discussions and for always staying enthusiastic and keeping me up to date with cool science ideas. I also want to thank **Joakim Hagel** for countless of discussions on bilayers. Furthermore, I want to thank the past and present members of the Ultrafast Quantum Dynamics Group at Chalmers and Philipps-Universität Marburg for all stimulating discussions over the years.

I am also grateful for the very successful experiment-theory collaborations together with the groups of **Alexey Chernikov** (TU Dresden) and **Andras**

Kis (EPFL), where besides Alexey and Andras, **Koloman Wagner**, **Fedele Tagarelli** and **Edoardo Lopriore** deserve my sincere gratitude.

I thank my examiner, **Andreas Isacsson**, for providing careful feedback on the thesis and co-supervisor **Paul Erhart** for useful discussions and the smooth collaboration with the Condensed Matter Physics graduate course over the years. In this context, I also thank **Julia Wiktor**.

My interest in condensed matter theory and the urge to pursue a PhD degree in such topics, was triggered during my graduate studies. Therefore, I would like to thank also my former thesis advisor **Henrik Johannesson** for all his encouragement. I am also happy to have had the opportunity to teach the last two rounds of his beloved course *Matematisk fysik* during my PhD studies.

Finally, a number of people contributed to fun distractions. Here, I thank past and current members of the PhD council, Chalmers Physics PhD Council, for sharing all the gossip and for contributing to the great atmosphere at the department. I also thank the Condensed Matter and Materials Theory Division for all the great Thursday fikas. The remainder of my gratitude goes to friends in and outside Academia and most importantly, my family. Tack!

Bibliography

[1] K. S. Novoselov. Nobel lecture: Graphene: Materials in the flatland. *Reviews of Modern Physics*, 83(3):837, 2011.

[2] K. F. Mak, C. Lee, J. Hone, J. Shan, and T. F. Heinz. Atomically thin MoS_2: A new direct-gap semiconductor. *Physical Review Letters*, 105:136805, 2010.

[3] Z. Wang, D. A. Rhodes, K. Watanabe, T. Taniguchi, J. C. Hone, J. Shan, and K. F. Mak. Evidence of high-temperature exciton condensation in two-dimensional atomic double layers. *Nature*, 574(7776):76–80, 2019.

[4] A. Kogar, Melinda S. Rak, S. Vig, A. A. Husain, F. Flicker, Y. I. Joe, L. Venema, G. J. MacDougall, T. C. Chiang, E. Fradkin, J. van Wezel, and P. Abbamonte. Signatures of exciton condensation in a transition metal dichalcogenide. *Science*, 358(6368):1314–1317, 2017.

[5] E. Y. Andrei, D. K. Efetov, P. Jarillo-Herrero, A. H. MacDonald, K. F. Mak, T. Senthil, E. Tutuc, A. Yazdani, and A. F. Young. The marvels of moiré materials. *Nature Reviews Materials*, 6(3):201–206, 2021.

[6] S. Brem and E. Malic. Terahertz fingerprint of monolayer Wigner crystals. *Nano Letters*, 2022.

[7] T. Mueller and E. Malic. Exciton physics and device application of two-dimensional transition metal dichalcogenide semiconductors. *npj 2D Materials and Applications*, 2(1):1–12, 2018.

[8] M. Cotrufo, L. Sun, J. Choi, A. Alù, and X. Li. Enhancing functionalities of atomically thin semiconductors with plasmonic nanostructures. *Nanophotonics*, 8(4):577–598, 2019.

[9] G. Wang, A. Chernikov, M. M. Glazov, T. F. Heinz, X. Marie, T. Amand, and B. Urbaszek. Colloquium: Excitons in atomically thin transition metal dichalcogenides. *Reviews of Modern Physics*, 90(2):021001, 2018.

[10] A. Chernikov, T. C. Berkelbach, H. M. Hill, A. Rigosi, Y. Li, B. Aslan, D. R. Reichman, M. S. Hybertsen, and T. F. Heinz. Exciton binding energy and nonhydrogenic Rydberg series in monolayer WS_2. *Physical Review Letters*, 113(7):076802, 2014.

[11] R. Perea-Causin, D. Erkensten, J. M. Fitzgerald, J. J. P. Thompson, R. Rosati, S. Brem, and E. Malic. Exciton optics, dynamics, and transport in atomically thin semiconductors. *APL Materials*, 10(10), 2022.

[12] D. Christiansen, M. Selig, G. Berghäuser, R. Schmidt, I. Niehues, R. Schneider, A. Arora, S. M. de Vasconcellos, R. Bratschitsch, E. Malic, and A. Knorr. Phonon sidebands in monolayer transition metal dichalcogenides. *Physical Review Letters*, 119(18):187402, 2017.

[13] S. Brem, A. Ekman, D. Christiansen, F. Katsch, M. Selig, C. Robert, X. Marie, B. Urbaszek, A. Knorr, and E. Malic. Phonon-assisted photoluminescence from indirect excitons in monolayers of transition-metal dichalcogenides. *Nano Letters*, 20(4):2849–2856, 2020.

[14] Z. Li, T. Wang, C. Jin, Z. Lu, Z. Lian, Y. Meng, M. Blei, S. Gao, T. Taniguchi, K. Watanabe, T. Ren, S. Tongay, L. Yang, D. Smirnov, T. Cao, and S.-F. Shi. Emerging photoluminescence from the dark-exciton phonon replica in monolayer WSe_2. *Nature Communications*, 10(1):2469, 2019.

[15] S. Brem, J. Zipfel, M. Selig, A. Raja, L. Waldecker, J. D. Ziegler, T. Taniguchi, K. Watanabe, A. Chernikov, and E. Malic. Intrinsic

lifetime of higher excitonic states in tungsten diselenide monolayers. *Nanoscale*, 11(25):12381–12387, 2019.

[16] Y.-H. Chan, J. B. Haber, M. H. Naik, J. B. Neaton, D. Y. Qiu, F. H. da Jornada, and S. G. Louie. Exciton lifetime and optical line width profile via exciton–phonon interactions: Theory and first-principles calculations for monolayer MoS_2. *Nano Letters*, 23(9):3971–3977, 2023.

[17] M. Selig, G. Berghäuser, A. Raja, P. Nagler, C. Schüller, T. F. Heinz, T. Korn, A. Chernikov, E. Malic, and A. Knorr. Excitonic linewidth and coherence lifetime in monolayer transition metal dichalcogenides. *Nature Communications*, 7(1):13279, 2016.

[18] G. Panzarini, L. C. Andreani, A. Armitage, D. Baxter, M. S. Skolnick, V. N. Astratov, J. S. Roberts, A. V. Kavokin, M. R. Vladimirova, and M. A. Kaliteevski. Exciton-light coupling in single and coupled semiconductor microcavities: Polariton dispersion and polarization splitting. *Physical Review B*, 59(7):5082, 1999.

[19] J. Kasprzak, M. Richard, S. Kundermann, A. Baas, P. Jeambrun, J. M. J. Keeling, F. M. Marchetti, M. H. Szymańska, R. André, J. L. Staehli, V. Savona, P. B. Littlewood, B. Deveaud, and L. S. Dang. Bose–Einstein condensation of exciton polaritons. *Nature*, 443(7110):409–414, 2006.

[20] J. M. Fitzgerald, J. J. P. Thompson, and E. Malic. Twist angle tuning of moiré exciton polaritons in van der Waals heterostructures. *Nano Letters*, 22(11):4468–4474, 2022.

[21] K. F. Mak, K. He, C. Lee, G. H. Lee, J. Hone, T. F. Heinz, and J. Shan. Tightly bound trions in monolayer MoS_2. *Nature Materials*, 12(3):207–211, 2013.

[22] J. S. Ross, S. Wu, H. Yu, N. J. Ghimire, A. M. Jones, G. Aivazian, J. Yan, D. G. Mandrus, D. Xiao, W. Yao, and X. Xu. Electrical control of neutral and charged excitons in a monolayer semiconductor. *Nature Communications*, 4(1):1474, 2013.

[23] H. C. Schneider, W. W. Chow, and S. W. Koch. Excitation-induced dephasing in semiconductor quantum dots. *Physical Review B*, 70(23):235308, 2004.

[24] F. Katsch, M. Selig, and A. Knorr. Exciton-scattering-induced dephasing in two-dimensional semiconductors. *Physical Review Letters*, 124(25):257402, 2020.

[25] N. Kumar, Q. Cui, F. Ceballos, D. He, Y. Wang, and H. Zhao. Exciton-exciton annihilation in $MoSe_2$ monolayers. *Physical Review B*, 89(12):125427, 2014.

[26] A. Suna. Kinematics of exciton-exciton annihilation in molecular crystals. *Physical Review B*, 1(4):1716, 1970.

[27] M. M. Ugeda, A. J. Bradley, S.-F. Shi, F. H. da Jornada, Y. Zhang, D. Y. Qiu, W. Ruan, S.-K. Mo, Z. Hussain, Z-X. Shen, F. Wang, S. G. Louie, and M. F. Crommie. Giant bandgap renormalization and excitonic effects in a monolayer transition metal dichalcogenide semiconductor. *Nature Materials*, 13(12):1091–1095, 2014.

[28] A. Steinhoff, J.-H. Kim, F. Jahnke, M. Rosner, D.-S. Kim, C. Lee, G. H. Han, M. S. Jeong, T. O. Wehling, and C. Gies. Efficient excitonic photoluminescence in direct and indirect band gap monolayer MoS_2. *Nano Letters*, 15(10):6841–6847, 2015.

[29] D. Erben, A. Steinhoff, C. Gies, G. Schönhoff, T. O. Wehling, and F. Jahnke. Excitation-induced transition to indirect band gaps in atomically thin transition-metal dichalcogenide semiconductors. *Physical Review B*, 98(3):035434, 2018.

[30] A. Steinhoff, E. Wietek, M. Florian, T. Schulz, T. Taniguchi, K. Watanabe, S. Zhao, A. Högele, F. Jahnke, and A. Chernikov. Exciton-exciton interactions in van der Waals heterobilayers. *arXiv preprint arXiv:2310.18328*, 2023.

[31] J. Zipfel, M. Kulig, R. Perea-Causin, S. Brem, J. D. Ziegler, R. Rosati, T. Taniguchi, K. Watanabe, M. M Glazov, E. Malic, and A. Chernikov. Exciton diffusion in monolayer semiconductors with suppressed disorder. *Physical Review B*, 101(11):115430, 2020.

[32] D. F. Cordovilla Leon, Z. Li, S. W. Jang, and P. B. Deotare. Hot exciton transport in WSe_2 monolayers. *Physical Review B*, 100(24):241401, 2019.

[33] L. Yuan, B. Zheng, J. Kunstmann, T. Brumme, A. B. Kuc, C. Ma, S. Deng, D. Blach, A. Pan, and L. Huang. Twist-angle-dependent interlayer exciton diffusion in $WS_2 - WSe_2$ heterobilayers. *Nature Materials*, 19(6):617–623, 2020.

[34] E. Malic, R. Perea-Causin, R. Rosati, D. Erkensten, and S. Brem. Exciton transport in atomically thin semiconductors. *Nature Communications*, 14(1):3430, 2023.

[35] C. Ciuti, V. Savona, C. Piermarocchi, A. Quattropani, and P. Schwendimann. Role of the exchange of carriers in elastic exciton-exciton scattering in quantum wells. *Physical Review B*, 58(12):7926, 1998.

[36] M. Katzer, M. Selig, D. Christiansen, M. V. Ballottin, P. C. M. Christianen, and A. Knorr. Impact of optically pumped nonequilibrium steady states on luminescence emission of atomically thin semiconductor excitons. *Physical Review Letters*, 131:146201, Oct 2023.

[37] D. Xiao, G.-B. Liu, W. Feng, X. Xu, and W. Yao. Coupled spin and valley physics in monolayers of MoS_2 and other group-VI dichalcogenides. *Physical Review Letters*, 108:196802, May 2012.

[38] A. Kormányos, G. Burkard, M. Gmitra, J. Fabian, V. Zólyomi, N. D. Drummond, and V. Fal'ko. $\mathbf{k}\cdot\mathbf{p}$ theory for two-dimensional transition metal dichalcogenide semiconductors. *2D Materials*, 2(2):022001, 2015.

[39] E. Malic, M. Selig, M. Feierabend, S. Brem, D. Christiansen, F. Wendler, A. Knorr, and G. Berghäuser. Dark excitons in transition metal dichalcogenides. *Physical Review Materials*, 2(1):014002, 2018.

[40] J. Madéo, M. K. L. Man, C. Sahoo, M. Campbell, V. Pareek, E. L. Wong, A. Al-Mahboob, N. S. Chan, A. Karmakar, B. M. K. Mariserla, X. Li, T. F. Heinz, T. Cao, and K. M. Dani. Directly visualizing the momentum-forbidden dark excitons and their dynamics in atomically thin semiconductors. *Science*, 370(6521):1199–1204, 2020.

[41] R. Wallauer, R. Perea-Causin, L. Münster, S. Zajusch, S. Brem, J. Güdde, K. Tanimura, K.-Q. Lin, R. Huber, E. Malic, and U. Höfer.

Momentum-resolved observation of exciton formation dynamics in monolayer WS_2. *Nano Letters*, 21(13):5867–5873, 2021.

[42] M. Selig, G. Berghäuser, M. Richter, R. Bratschitsch, A. Knorr, and E. Malic. Dark and bright exciton formation, thermalization, and photoluminescence in monolayer transition metal dichalcogenides. *2D Materials*, 5(3):035017, 2018.

[43] G. Berghäuser, P. Steinleitner, P. Merkl, R. Huber, A. Knorr, and E. Malic. Mapping of the dark exciton landscape in transition metal dichalcogenides. *Physical Review B*, 98(2):020301, 2018.

[44] D. Schmitt, J. P. Bange, W. Bennecke, A. AlMutairi, G. Meneghini, K. Watanabe, T. Taniguchi, D. Steil, D. R. Luke, R. T. Weitz, S. Steil, G. S. M. Jansen, S. Brem, E. Malic, S. Hofmann, M. Reutzel, and S. Mathias. Formation of moiré interlayer excitons in space and time. *Nature*, 608(7923):499–503, 2022.

[45] Y. Cao, V. Fatemi, S. Fang, K. Watanabe, T. Taniguchi, E. Kaxiras, and P. Jarillo-Herrero. Unconventional superconductivity in magic-angle graphene superlattices. *Nature*, 556(7699):43–50, 2018.

[46] H. Li, S. Li, E. C. Regan, D. Wang, W. Zhao, S. Kahn, K. Yumigeta, M. Blei, T. Taniguchi, K. Watanabe, S. Tongay, A. Zettl, M. F. Crommie, and F. Wang. Imaging two-dimensional generalized Wigner crystals. *Nature*, 597(7878):650–654, 2021.

[47] Y. Xu, S. Liu, D. A. Rhodes, K. Watanabe, T. Taniguchi, J. Hone, V. Elser, K. F. Mak, and J. Shan. Correlated insulating states at fractional fillings of moiré superlattices. *Nature*, 587(7833):214–218, 2020.

[48] Y. Zeng, Z. Xia, R. Dery, K. Watanabe, T. Taniguchi, J. Shan, and K. F. Mak. Exciton density waves in Coulomb-coupled dual moiré lattices. *Nature Materials*, 22(2):175–179, 2023.

[49] A. J. Campbell, M. Brotons-Gisbert, H. Baek, V. Vitale, T. Taniguchi, K. Watanabe, J. Lischner, and B. D. Gerardot. Exciton-polarons in the presence of strongly correlated electronic states in a $MoSe_2/WSe_2$ moiré superlattice. *npj 2D Materials and Applications*, 6(1):79, 2022.

[50] P. Rivera, J. R. Schaibley, A. M. Jones, J. S. Ross, S. Wu, G. Aivazian, P. Klement, K. Seyler, G. Clark, N. J. Ghimire, J. Yan, D. G. Mandrus, W. Yao, and X. Xu. Observation of long-lived interlayer excitons in monolayer $MoSe_2$-WSe_2 heterostructures. *Nature Communications*, 6(1):1–6, 2015.

[51] S. Ovesen, S. Brem, C. Linderälv, M. Kuisma, T. Korn, P. Erhart, M. Selig, and E. Malic. Interlayer exciton dynamics in van der Waals heterostructures. *Communications Physics*, 2(1):1–8, 2019.

[52] Z. Sun, A. Ciarrocchi, F. Tagarelli, M. Gonzalez, F. Juan, K. Watanabe, T. Taniguchi, and A. Kis. Excitonic transport driven by repulsive dipolar interaction in a van der Waals heterostructure. *Nature Photonics*, 16:79–85, 2021.

[53] L. A. Jauregui, A. Y. Joe, K. Pistunova, D. S. Wild, A. A. High, Y. Zhou, G. Scuri, K. De Greve, A. Sushko, C.-H. Yu, T. Taniguchi, K. Watanabe, D. J. Needleman, M. D. Lukin, H. Park, and P. Kim. Electrical control of interlayer exciton dynamics in atomically thin heterostructures. *Science*, 366(6467):870–875, 2019.

[54] M. Combescot, R. Combescot, and F. Dubin. Bose–Einstein condensation and indirect excitons: a review. *Reports on Progress in Physics*, 80(6):066501, 2017.

[55] F. Katsch, M. Selig, A. Carmele, and A. Knorr. Theory of exciton–exciton interactions in monolayer transition metal dichalcogenides. *physica status solidi (b)*, 255(12):1800185, 2018.

[56] A. L. Ivanov and H. Haug. Self-consistent theory of the biexciton optical nonlinearity. *Physical Review B*, 48(3):1490, 1993.

[57] T. Usui. Excitations in a high density electron gas. i. *Progress of Theoretical Physics*, 23(5):787–798, 1960.

[58] H. Haug and S. W. Koch. *Quantum theory of the optical and electronic properties of semiconductors*. World Scientific Publishing Company, 2009.

[59] M. O. Scully and M. S. Zubairy. Quantum optics, 1999.

[60] J. J. P. Thompson, S. Brem, H. Fang, C. Antón-Solanas, B. Han, H. Shan, S. P. Dash, W. Wieczorek, C. Schneider, and E. Malic. Valley-exchange coupling probed by angle-resolved photoluminescence. *Nanoscale Horizons*, 7(1):77–84, 2022.

[61] T. Winzer, A. Knorr, and E. Malic. Carrier multiplication in graphene. *Nano Letters*, 10(12):4839–4843, 2010.

[62] F. Wang, Y. Wu, M. S. Hybertsen, and T. F. Heinz. Auger recombination of excitons in one-dimensional systems. *Physical Review B*, 73(24):245424, 2006.

[63] N. S. Rytova. Screened potential of a point charge in a thin film. *Moscow University Physics Bulletin*, 3(30), 1967.

[64] L. V. Keldysh. Coulomb interaction in thin semiconductor and semimetal films. *Soviet Journal of Experimental and Theoretical Physics Letters*, 29:658, 1979.

[65] P. Cudazzo, I. V. Tokatly, and A. Rubio. Dielectric screening in two-dimensional insulators: Implications for excitonic and impurity states in graphane. *Physical Review B*, 84(8):085406, 2011.

[66] M. L. Trolle, T. G. Pedersen, and V. Véniard. Model dielectric function for 2D semiconductors including substrate screening. *Scientific Reports*, 7(1):1–9, 2017.

[67] P. Merkl, F. Mooshammer, P. Steinleitner, A. Girnghuber, K.-Q. Lin, P. Nagler, J. Holler, C. Schüller, J. M. Lupton, T. Korn, S. Ovesen, S. Brem, E. Malic, and R. Huber. Ultrafast transition between exciton phases in van der Waals heterostructures. *Nature Materials*, 18(7):691–696, 2019.

[68] A. Laturia, M. L. Van de Put, and W. G. Vandenberghe. Dielectric properties of hexagonal boron nitride and transition metal dichalcogenides: from monolayer to bulk. *npj 2D Materials and Applications*, 2(1):6, 2018.

[69] R. Geick, C. H. Perry, and G. J. P. R. Rupprecht. Normal modes in hexagonal boron nitride. *Physical Review*, 146(2):543, 1966.

[70] S. Latini, T. Olsen, and K. S. Thygesen. Excitons in van der Waals heterostructures: The important role of dielectric screening. *Physical Review B*, 92(24):245123, 2015.

[71] D. Y. Qiu, F. H. da Jornada, and S. G. Louie. Screening and many-body effects in two-dimensional crystals: Monolayer MoS_2. *Physical Review B*, 93(23):235435, 2016.

[72] M. Kira and S. W. Koch. Many-body correlations and excitonic effects in semiconductor spectroscopy. *Progress in Quantum Electronics*, 30(5):155–296, 2006.

[73] L. J. Sham and T. M. Rice. Many-particle derivation of the effective-mass equation for the Wannier exciton. *Physical Review*, 144(2):708, 1966.

[74] J. Frenkel. On the transformation of light into heat in solids. i. *Physical Review*, 37(1):17, 1931.

[75] R. Schuster, M. Knupfer, and H. Berger. Exciton band structure of pentacene molecular solids: breakdown of the frenkel exciton model. *Physical Review Letters*, 98(3):037402, 2007.

[76] S. Brem, M. Selig, G. Berghäuser, and E. Malic. Exciton relaxation cascade in two-dimensional transition metal dichalcogenides. *Scientific Reports*, 8(1):1–8, 2018.

[77] M. Feierabend, G. Berghäuser, A. Knorr, and E. Malic. Proposal for dark exciton based chemical sensors. *Nature communications*, 8(1):14776, 2017.

[78] T. Marumori, M. Yamamura, and A. Tokunaga. On the "anharmonic effects" on the collective oscillations in spherical even nuclei. i. *Progress of Theoretical Physics*, 31(6):1009–1025, 1964.

[79] E. Hanamura. Theory of the high density exciton. i. *Journal of the Physical Society of Japan*, 29(1):50–57, 1970.

[80] S. Brem, K.-Q. Lin, R. Gillen, J. M. Bauer, J. Maultzsch, J. M. Lupton, and E. Malic. Hybridized intervalley moiré excitons and flat bands in twisted WSe_2 bilayers. *Nanoscale*, 12(20):11088–11094, 2020.

[81] T. Siday, F. Sandner, S. Brem, M. Zizlsperger, R. Perea-Causin, F. Schiegl, S. Nerreter, M. Plankl, P. Merkl, F. Mooshammer, M. A. Huber, E. Malic, and R. Huber. Ultrafast nanoscopy of high-density exciton phases in WSe_2. *Nano Letters*, 22(6):2561–2568, 2022.

[82] G. Rochat, C. Ciuti, V. Savona, C. Piermarocchi, A. Quattropani, and P. Schwendimann. Excitonic Bloch equations for a two-dimensional system of interacting excitons. *Physical Review B*, 61:13856–13862, 2000.

[83] J. Choi, W.-T. Hsu, L.-S. Lu, L. Sun, H.-Y. Cheng, M.-H. Lee, J. Quan, K. Tran, C.-Y. Wang, M. Staab, K. Jones, T. Taniguchi, K. Watanabe, M.-W. Chu, S. Gwo, S. Kim, C.-K. Shih, X. Li, and W.-H. Chang. Moiré potential impedes interlayer exciton diffusion in van der Waals heterostructures. *Science Advances*, 6(39):eaba8866, 2020.

[84] G. Moody, C. K. Dass, K. Hao, C.-H. Chen, L.-J. Li, A. Singh, K. Tran, G. Clark, X. Xu, G. Berghäuser, E. Malic, A. Knorr, and X. Li. Intrinsic homogeneous linewidth and broadening mechanisms of excitons in monolayer transition metal dichalcogenides. *Nature Communications*, 6(1):1–6, 2015.

[85] P. Nagler, G. Plechinger, M. V. Ballottin, A. Mitioglu, S. Meier, N. Paradisio, C. Strunk, A. Chernikov, P. C. M. Christianen, C. Schüller, and T. Korn. Interlayer exciton dynamics in a dichalcogenide monolayer heterostructure. *2D Materials*, 4(2):025112, 2017.

[86] C. Trovatello, F. Katsch, Q. Li, X. Zhu, A. Knorr, G. Cerullo, and S. Dal Conte. Disentangling many-body effects in the coherent optical response of 2D semiconductors. *Nano Letters*, 22(13):5322–5329, 2022.

[87] M. Combescot, O. Betbeder-Matibet, and R. Combescot. Exciton-exciton scattering: Composite boson versus elementary boson. *Physical Review B*, 75:174305, 2007.

[88] C. Schindler and R. Zimmermann. Analysis of the exciton-exciton interaction in semiconductor quantum wells. *Physical Review B*, 78(4):045313, 2008.

[89] D. Erkensten, S. Brem, and E. Malic. Exciton-exciton interaction in transition metal dichalcogenide monolayers and van der Waals heterostructures. *Physical Review B*, 103:045426, Jan 2021.

[90] D. Erkensten, S. Brem, R. Perea-Causin, and E. Malic. Microscopic origin of anomalous interlayer exciton transport in van der Waals heterostructures. *Physical Review Materials*, 6(9):094006, 2022.

[91] D. Erkensten, S. Brem, R. Perea-Causin, J. Hagel, F. Tagarelli, E. Lopriore, A. Kis, and E. Malic. Electrically tunable dipolar interactions between layer-hybridized excitons. *Nanoscale*, 2023.

[92] F. Tagarelli, E. Lopriore, D. Erkensten, R. Perea-Causin, S. Brem, J. Hagel, Z. Sun, G. Pasquale, K. Watanabe, T. Taniguchi, E. Malic, and A. Kis. Electrical control of hybrid exciton transport in a van der Waals heterostructure. *Nature Photonics*, 17:615–621, 2023.

[93] F. Tassone and Y. Yamamoto. Exciton-exciton scattering dynamics in a semiconductor microcavity and stimulated scattering into polaritons. *Physical Review B*, 59:10830–10842, 1999.

[94] V. Shahnazaryan, I. Iorsh, I. A. Shelykh, and O. Kyriienko. Exciton-exciton interaction in transition-metal dichalcogenide monolayers. *Physical Review B*, 96:115409, 2017.

[95] A. K. Geim and I. V. Grigorieva. Van der Waals heterostructures. *Nature*, 499(7459):419–425, 2013.

[96] R. Gillen and J. Maultzsch. Interlayer excitons in $MoSe_2/WSe_2$ heterostructures from first principles. *Physical Review B*, 97(16):165306, 2018.

[97] J. Hagel, S. Brem, C. Linderälv, P. Erhart, and E. Malic. Exciton landscape in van der Waals heterostructures. *Physical Review Research*, 3(4):043217, 2021.

[98] M. Troue, J. Figueiredo, L. Sigl, C. Paspalides, M. Katzer, T. Taniguchi, K. Watanabe, M. Selig, A. Knorr, U. Wurstbauer, and A. W. Holleitner. Extended spatial coherence of interlayer excitons in $MoSe_2/WSe_2$ heterobilayers. *Physical Review Letters*, 131:036902, 2023.

[99] S. Brem. *Microscopic Theory of Exciton Dynamics in Two-Dimensional Materials*. PhD thesis, Chalmers University of Technology, 2021.

[100] Z. Jin, X. Li, J. T. Mullen, and K. W. Kim. Intrinsic transport properties of electrons and holes in monolayer transition-metal dichalcogenides. *Physical Review B*, 90:045422, 2014.

[101] T. Deilmann and K. S. Thygesen. Finite-momentum exciton landscape in mono-and bilayer transition metal dichalcogenides. *2D Materials*, 6(3):035003, 2019.

[102] Z. Wang, Y.-H. Chiu, K. Honz, K. F. Mak, and J. Shan. Electrical tuning of interlayer exciton gases in wse2 bilayers. *Nano Letters*, 18(1):137–143, 2018.

[103] J. Förste, N. V. Tepliakov, S. Y. Kruchinin, J. Lindlau, V. Funk, M. Förg, K. Watanabe, T. Taniguchi, A. S. Baimuratov, and A. Högele. Exciton g-factors in monolayer and bilayer WSe_2 from experiment and theory. *Nature Communications*, 11(1):4539, 2020.

[104] M. M. Altaiary, E. Liu, C.-T. Liang, F.-C. Hsiao, J. van Baren, T. Taniguchi, K. Watanabe, N. M. Gabor, Y.-C. Chang, and C. H. Lui. Electrically switchable intervalley excitons with strong two-phonon scattering in bilayer WSe_2. *Nano Letters*, 22(5):1829–1835, 2022.

[105] M. Kira and S. W. Koch. *Semiconductor Quantum Optics*. Cambridge University Press, 2011.

[106] G. Röpke and R. Der. The influence of two-particle states (excitons) on the dielectric function of the electron—hole plasma. *physica status solidi (b)*, 92(2):501–510, 1979.

[107] N. Bohr and J. Lindhard. *Electron capture and loss by heavy ions penetrating through matter*, volume 28. Dan. Mat. Fys, 1954.

[108] L. Hedin. New method for calculating the one-particle Green's function with application to the electron-gas problem. *Physical Review*, 139:A796–A823, 1965.

[109] O. Kyriienko, E. B. Magnusson, and I. A. Shelykh. Spin dynamics of cold exciton condensates. *Physical Review B*, 86:115324, Sep 2012.

[110] C. Louca, A. Genco, S. Chiavazzo, T. P. Lyons, S. Randerson, C. Trovatello, P. Claronino, R. Jayaprakash, X. Hu, J. Howarth, K. Watanabe, T. Taniguchi, S. Dal Conte, R. Gorbachev, D. G. Lidzey, G. Cerullo, O. Kyriienko, and A. I. Tartakovskii. Interspecies exciton interactions lead to enhanced nonlinearity of dipolar excitons and polaritons in MoS_2 homobilayers. *Nature Communications*, 14(1):3818, 2023.

[111] D. Unuchek, A. Ciarrocchi, A. Avsar, K. Watanabe, T. Taniguchi, and A. Kis. Room-temperature electrical control of exciton flux in a van der Waals heterostructure. *Nature*, 560(7718):340–344, 2018.

[112] A. Steinhoff, M. Florian, M. Rösner, G. Schönhoff, T. O. Wehling, and F. Jahnke. Exciton fission in monolayer transition metal dichalcogenide semiconductors. *Nature Communications*, 8(1):1–11, 2017.

[113] F. Cadiz, C. Robert, E. Courtade, M. Manca, L. Martinelli, T. Taniguchi, K. Watanabe, T. Amand, A. C. H. Rowe, D. Paget, B. Urbaszek, and X. Marie. Exciton diffusion in WSe_2 monolayers embedded in a van der Waals heterostructure. *Applied Physics Letters*, 112(15), 2018.

[114] A. Raja, L. Waldecker, J. Zipfel, Y. Cho, S. Brem, J. D. Ziegler, M. Kulig, T. Taniguchi, K. Watanabe, E. Malic, T. F. Heinz, T. C. Berkelbach, and A. Chernikov. Dielectric disorder in two-dimensional materials. *Nature Nanotechnology*, 14(9):832–837, 2019.

[115] R. Perea-Causin, S. Brem, R. Rosati, R. Jago, M. Kulig, J. D. Ziegler, J. Zipfel, A. Chernikov, and E. Malic. Exciton propagation and halo formation in two-dimensional materials. *Nano Letters*, 19(10):7317–7323, 2019.

[116] M. Kulig, J. Zipfel, P. Nagler, S. Blanter, C. Schüller, T. Korn, N. Paradiso, M. M. Glazov, and A. Chernikov. Exciton diffusion and halo effects in monolayer semiconductors. *Physical Review Letters*, 120:207401, May 2018.

[117] K. Wagner, J. Zipfel, R. Rosati, E. Wietek, J. D. Ziegler, S. Brem, R. Perea-Causin, T. Taniguchi, K. Watanabe, M. M. Glazov, E. Malic, and A. Chernikov. Nonclassical exciton diffusion in monolayer WSe_2. *Physical Review Letters*, 127:076801, Aug 2021.

[118] Roberto Rosati, R. Perea-Causin, S. Brem, and E. Malic. Negative effective excitonic diffusion in monolayer transition metal dichalcogenides. *Nanoscale*, 12(1):356–363, 2020.

[119] L. Yuan and L. Huang. Exciton dynamics and annihilation in WS_2 2D semiconductors. *Nanoscale*, 7(16):7402–7408, 2015.

[120] O. Hess and T. Kuhn. Maxwell-Bloch equations for spatially inhomogeneous semiconductor lasers. I. Theoretical formulation. *Physical Review A*, 54:3347–3359, 1996.

[121] A. L. Ivanov. Quantum diffusion of dipole-oriented indirect excitons in coupled quantum wells. *Europhysics Letters*, 59(4):586, 2002.

[122] R. Rosati, R. Schmidt, S. Brem, R. Perea-Causin, I. Niehues, J. Kern, J. A. Preuß, R. Schneider, S. Michaelis de Vasconcellos, R. Bratschitsch, and E. Malic. Dark exciton anti-funneling in atomically thin semiconductors. *Nature Communications*, 12(1):1–7, 2021.

[123] D. Y. Qiu, G. Cohen, D. Novichkova, and S. Refaely-Abramson. Signatures of dimensionality and symmetry in exciton band structure: Consequences for exciton dynamics and transport. *Nano Letters*, 21(18):7644–7650, 2021.

[124] J. Wang, Q. Shi, E.-M. Shih, L. Zhou, W. Wu, Y. Bai, D. Rhodes, K. Barmak, J. Hone, C. R. Dean, and X-Y. Zhu. Diffusivity reveals three distinct phases of interlayer excitons in $MoSe_2/WSe_2$ heterobilayers. *Physical Review Letters*, 126:106804, Mar 2021.

[125] Y. Shimazaki, I. Schwartz, K. Watanabe, T. Taniguchi, M. Kroner, and A. Imamoğlu. Strongly correlated electrons and hybrid excitons in a moiré heterostructure. *Nature*, 580(7804):472–477, 2020.

[126] Q. Shi, E.-M. Shih, D. Rhodes, B. Kim, K. Barmak, K. Watanabe, T. Taniguchi, Z. Papić, D. A. Abanin, J. Hone, and C. R. Dean. Bilayer

WSe_2 as a natural platform for interlayer exciton condensates in the strong coupling limit. *Nature Nanotechnology*, 17(6):577–582, 2022.

[127] T. Winzer and E. Malic. Impact of Auger processes on carrier dynamics in graphene. *Physical Review B*, 85(24):241404, 2012.

[128] X.-X. Zhang, Y. You, S. Y. F. Zhao, and T. F. Heinz. Experimental evidence for dark excitons in monolayer WSe_2. *Physical Review Letters*, 115(25):257403, 2015.

[129] K.-Q. Lin, C. S. Ong, S. Bange, P. E. Faria Junior, B. Peng, J. D. Ziegler, J. Zipfel, C. Bäuml, N. Paradiso, K. Watanabe, T. Taniguchi, C. Strunk, B. Monserrat, J. Fabian, A. Chernikov, D. Y. Qiu, S. G. Louie, and J. M. Lupton. Narrow-band high-lying excitons with negative-mass electrons in monolayer WSe_2. *Nature Communications*, 12(1):1–8, 2021.

[130] K.-Q. Lin, P. E. Faria Junior, J. M. Bauer, B. Peng, B. Monserrat, M. Gmitra, J. Fabian, S. Bange, and J. M. Lupton. Twist-angle engineering of excitonic quantum interference and optical nonlinearities in stacked 2D semiconductors. *Nature Communications*, 12(1):1–7, 2021.

[131] K.-Q. Lin, P. E. Faria Junior, R. Hübner, J. D. Ziegler, J. M. Bauer, F. Buchner, M. Florian, F. Hofmann, K. Watanabe, T. Taniguchi, J. Fabian, A. Steinhoff, A. Chernikov, S. Bange, and J. M. Lupton. Ultraviolet interlayer excitons in bilayer WSe_2. *Nature Nanotechnology*, 2023.

[132] B. Han, C. Robert, E. Courtade, M. Manca, S. Shree, T. Amand, P. Renucci, T. Taniguchi, K. Watanabe, X. Marie, L. E. Golub, M. M. Glazov, and B. Urbaszek. Exciton states in monolayer $MoSe_2$ and $MoTe_2$ probed by upconversion spectroscopy. *Physical Review X*, 8:031073, 2018.

[133] D. Erkensten, S. Brem, K. Wagner, R. Gillen, R. Perea-Causin, J. D. Ziegler, T. Taniguchi, K. Watanabe, J. Maultzsch, A. Chernikov, and E. Malic. Dark exciton-exciton annihilation in monolayer WSe_2. *Physical Review B*, 104(24):L241406, 2021.

[134] S. Deng, E. Shi, L. Yuan, L. Jin, L. Dou, and L. Huang. Long-range exciton transport and slow annihilation in two-dimensional hybrid perovskites. *Nature Communications*, 11(1):1–8, 2020.

[135] E. Maggiolini, L. Polimeno, F. Todisco, A. Di Renzo, B. Han, M. De Giorgi, V. Ardizzone, C. Schneider, R. Mastria, A. Cannavale, M. Puggliese, L. De Marco, A. Rizzo, V. Maiorano, G. Gigli, D. Gerace, Sanvitto D., and D. Ballarini. Strongly enhanced light–matter coupling of monolayer WS_2 from a bound state in the continuum. *Nature Materials*, 22:964–969, 2023.

[136] J. Zhao, A. Fieramosca, K. Dini, R. Bao, W. Du, R. Su, Y. Luo, W. Zhao, D. Sanvitto, T. C. H. Liew, and Q. Xiong. Exciton polariton interactions in van der Waals superlattices at room temperature. *Nature Communications*, 14(1):1512, 2023.

[137] D. Beret, I. Paradisanos, H. Lamsaadi, Z. Gan, E. Najafidehaghani, A. George, T. Lehnert, J. Biskupek, U. Kaiser, S. Shree, A. Estrada-Real, D. Lagarde, X. Marie, P. Renucci, K. Watanabe, T. Taniguchi, S. Weber, V. Paillard, J-M. Lombez, L. Poumirol, A. Turchanin, and B. Urbaszek. Exciton spectroscopy and unidirectional transport in $MoSe_2$-WSe_2 lateral heterostructures encapsulated in hexagonal boron nitride. *npj 2D Materials and Applications*, 6(1):84, 2022.

[138] L. Yuan, B. Zheng, Q. Zhao, R. Kempt, T. Brumme, A. B. Kuc, C. Ma, S. Deng, A. Pan, and L. Huang. Strong dipolar repulsion of one-dimensional interfacial excitons in monolayer lateral heterojunctions. *ACS Nano*, 17(16):15379–15387, 2023.

[139] R. Rosati, I. Paradisanos, L. Huang, Z. Gan, A. George, K. Watanabe, T. Taniguchi, L. Lombez, P. Renucci, A. Turchanin, B. Urbaszek, and E. Malic. Interface engineering of charge-transfer excitons in 2D lateral heterostructures. *Nature Communications*, 14(1):2438, 2023.

[140] K. W. Lau, Calvin, Z. Gong, Y. Hongyi, and W. Yao. Interface excitons at lateral heterojunctions in monolayer semiconductors. *Physical Review B*, 98:115427, 2018.

[141] J. K. König, J. M. Fitzgerald, J. Hagel, D. Erkensten, and E. Malic. Interlayer exciton polaritons in homobilayers of transition metal dichalcogenides. *2D Materials*, 10(2):025019, 2023.

[142] B. Datta, M. Khatoniar, P. Deshmukh, F. Thouin, R. Bushati, S. De Liberato, S. K. Cohen, and V. M. Menon. Highly nonlinear dipolar exciton-polaritons in bilayer MoS_2. *Nature Communications*, 13(1):6341, 2022.

[143] B. Paredes, A. Widera, V. Murg, O. Mandel, S. Fölling, I. Cirac, G. V. Shlyapnikov, T. W. Hänsch, and I. Bloch. Tonks–Girardeau gas of ultracold atoms in an optical lattice. *Nature*, 429(6989):277–281, 2004.

[144] R. Ołdziejewski, A. Chiocchetta, J. Knörzer, and R. Schmidt. Excitonic Tonks-Girardeau and charge density wave phases in monolayer semiconductors. *Physical Review B*, 106(8):L081412, 2022.

[145] K. F. Mak and J. Shan. Semiconductor moiré materials. *Nature Nanotechnology*, 17(7):686–695, 2022.

[146] S. Brem, C. Linderälv, P. Erhart, and E. Malic. Tunable phases of moiré excitons in van der Waals heterostructures. *Nano Letters*, 20(12):8534–8540, 2020.

[147] M. Brotons-Gisbert, H. Baek, A. Campbell, K. Watanabe, T. Taniguchi, and B. D. Gerardot. Moiré-trapped interlayer trions in a charge-tunable $WSe_2/MoSe_2$ heterobilayer. *Physical Review X*, 11:031033, 2021.

[148] H. Baek, M. Brotons-Gisbert, Z. X. Koong, A. Campbell, M. Rambach, K. Watanabe, T. Taniguchi, and B. D. Gerardot. Highly energy-tunable quantum light from moiré-trapped excitons. *Science Advances*, 6(37):eaba8526, 2020.

[149] M. H. Naik, E. C. Regan, Z. Zhang, Y.-H. Chan, Z Li, D. Wang, Y. Yoon, C. S. Ong, W. Zhao, S. Zhao, M. I. B. Utama, B. Gao, X. Wei, M. Sayyad, K. Yumigeta, K. Watanabe, T. Taniguchi, S. Tongay, F. H. da Jornada, F. Wang, and S. G. Louie. Intralayer charge-transfer moiré excitons in van der Waals superlattices. *Nature*, 609(7925):52–57, 2022.

[150] H. Pan, F. Wu, and S. Das Sarma. Quantum phase diagram of a moiré-Hubbard model. *Physical Review B*, 102:201104, 2020.

[151] Y. Zhou, J. Sung, E. Brutschea, I. Esterlis, Y. Wang, G. Scuri, R. J. Gelly, H. Heo, T. Taniguchi, K. Watanabe, G. Zarand, M. D. Lukin,

P. Kim, E. Demler, and H. Park. Bilayer Wigner crystals in a transition metal dichalcogenide heterostructure. *Nature*, 595(7865):48–52, 2021.

[152] N. Götting, F. Lohof, and C. Gies. Moiré-Bose-Hubbard model for interlayer excitons in twisted transition metal dichalcogenide heterostructures. *Physical Review B*, 105:165419, 2022.

[153] A. Julku. Nonlocal interactions and supersolidity of moiré excitons. *Physical Review B*, 106(3):035406, 2022.

[154] S. Brem and E. Malic. Bosonic delocalization of dipolar moiré excitons. *Nano Letters*, 2023.

[155] R. Huang, D. Yu, and W. Yao. Majorana fermions on the domain wall of marginally twisted bilayer of transition metal dichalcogenides. *Physical Review B*, 108:115307, 2023.

[156] C. Zerba, C. Kuhlenkamp, A. Imamoğlu, and M. Knap. Realizing topological superconductivity in tunable Bose-Fermi mixtures with transition metal dichalcogenide heterostructures. *arXiv preprint arXiv:2310.10720*, 2023.